Design and Optimization of Colloidal Quantum Dot Solids for Enhanced Charge Transport and Photovoltaics

by

Sangjin Lee

B.S., Kyoto University, Japan (2006)
M.S., Kyoto University, Japan (2008)

Submitted to the Department of Materials Science and Engineering
in partial fulfillment of the requirements for the degree of

Doctor of Philosophy

at the

MASSACHUSETTS INSTITUTE OF TECHNOLOGY

June 2016

Author .....
Department of Materials Science and Engineering
May 13, 2016

Certified by .....
Jeffrey C. Grossman
Professor of Materials Science and Engineering
Thesis Supervisor

Accepted by .....
Donald R. Sadoway
John F. Elliott Professor of Materials Science and Engineering
Chair, Departmental Committee on Graduate Students

Design and Optimization of Colloidal Quantum Dot Solids for Enhanced Charge Transport and Photovoltaics

by

Sangjin Lee

Submitted to the Department of Materials Science and Engineering
on May 13, 2016, in partial fulfillment of the
requirements for the degree of
Doctor of Philosophy

Abstract

Colloidal quantum dots (CQDs) have attracted much attention due to their distinctive optical properties such as wide spectral responses and tunable absorption spectra with simple size control. These properties, together with the advantages of solution processing and superior robustness to organic materials, have motivated the recent investigation of CQD-based solar cells, which have seen rapid growth in power conversion efficiency in just the last 10 years, to a current record of over 10%. However, in order to continue to push the efficiencies higher, a better understanding of the charge transport phenomena in CQD films is needed. While the carrier transport mechanisms between isolated molecules have been explored theoretically and the device-scale mobility of CQD layers has been characterized using experimental measurements such as time-of-flight analysis and field-effect-transistor measurements, a systematic study of the connection between these two distinct scales is required in order to provide crucial information regarding how CQD layers with higher charge carrier mobility can be achieved.

While a few strategies such as ligand exchanges, band-like transport, and trap-state-mediated transport have been suggested to enhance the charge carrier mobility, inhomogeneity in CQD solids has been considered a source of the mobility degradation because the electronic properties in individual CQDs may have dispersions introduced in the synthesis and/or in the deposition process, leading to the deviations of the localized energy states from the regular positions or the average energy levels. Here, we suggest that control over such design factors in CQD solids can provide important pathways for improvements in device efficiencies as well as the charge carrier mobility. In particular, we have focused on the polydispersity in CQDs, which normally lies in the range of 5-15%. The effect of size-dispersion in CQD solids on the charge carrier mobility was computed using charge hopping transport models. The experimental film deposition processes were replicated using a molecular dynamics simulation where the equilibrium positions of CQDs with a given radii distribution were determined under a granular potential. The radii and positions of the CQDs were then used in the charge hopping transport simulator where the carrier mobility

was estimated. We observed large decreases (up to 70%) in electron mobility for typical experimental polydispersity (about 10%) in CQD films. These large degradations in hopping charge transport were investigated using transport vector analysis with which we suggested that the site energy differences raised the portion of the off-axis rate of charge transport to the electric field direction. Furthermore, we have shown that controlling the size distribution remarkably impacts the charge carrier mobility and we suggested that tailored and potentially experimentally achievable re-arrangement of the CQD size ensemble can mediate the mobility drops even in highly dispersive cases, and presents an avenue towards improved charge transport. We then studied the degradation in CQD solar cells with respect to the polydispersity and how these enhanced charge transport from re-design of CQD solids can boost the photovoltaic performances. In addition, we estimated the potential in the binary CQD solids in terms of their improved charge transport and efficient light absorption. Combined with the accurate size-dependent optical absorption model for CQDs, our hopping model confirmed that the inclusion of smaller CQDs could enhance both the charge transport and the solar light absorption, leading to the enhanced average charge generation rates and solar cell performance.

Thesis Supervisor: Jeffrey C. Grossman
Title: Professor of Materials Science and Engineering

Acknowledgments

I would like to thank my thesis advisor, Professor Jeffrey C. Grossman. He was the best leader I have ever met personally. He always inspired me with his insight and expertise on my research and helped all of us, group members, enjoy the big part of academic journey in his group. I think he knows well how to motivate people, including myself, and it was so lucky for me to join his group. 5 years in his group were really valuable time not only for my research career but also for my life. I also thank Professor Harry Tuller. I could have a great chance to take his classes where I established the knowledge on device physics. His questions in the thesis committee meeting helped me to improve the logic, on which all the contents of this thesis are based. I personally respect his energy and passion on educating and fostering young researchers. And I gratefully thank Professor Ju Li. Even though he joined my thesis committee after my 4th year, his questions played a critical role in validating the method I developed, leading to an excellent chance for me to inspire the community with my own code. I thank all Grossman group members for building supportive atmosphere in the offices, for the valuable academic discussions we had, and for having a great time with in every group retreat. I specially thank Brent. We were roommates by chance, joined the same group, and work together through all the exams and meetings in MIT. He's been a good friend, a great colleague, and a friendly drinker. I will not forget cocktails he made for me. I want to thank David Zhitomirsky for his support. His advices accelerated the progress of my research significantly and helped me finish Ph.D this year. I want to thank David Strubbe, Yun Liu and Huashan Li for valuable discussions and excellent questions I got in the group meetings. Their intuitions and insights was great help in developing my research. I am grateful to Shreya Dave and Grace Han for their warm welcome when I moved from the other corridor and for the conversations on research and academic life. I also thank Yun Liu (Yunior) for his all the efforts and services on cluster maintenance, and for the chatting about clusters managements as well as quantum dots. I thank Jeongyun Kim for all her encouragements and guidances as a senior,

which helped me a lot to clear the requirements and milestones. I want to express my gratitude to all my friend I have met in Boston area. They fulfilled my life here for the last five years and encouraged me to keep striding through this academic milestones. I especially thank Sehoon Chang, Sungho Choi and their family for all the great time we had in Boston. I thank my family members for their support and patience. They always encouraged me to finally achieve this academic goal. I specially thank my wife, Haejo, for her devotion to family. For the last half of my stay in US, she had to take care of our son by herself in Korea even though she was working. I really appreciate her support and patience. Last, I want to thank my son, Jaehee, for all his smiles, every word he says and being our son.

Contents

List of Figures

List of Tables

Chapter 1

Introduction

Due to the peculiar optoelectronic properties combined with solution-processability, colloidal quantum dots (CQDs) have attracted much attention [6–8] and have been applied to a variety of optoelectronic devices such as solar cells, [9–15] light-emitting devices, [16–19] and photodetectors. [20–22] Although recent improvements in such CQD devices have shown significantly enhanced efficiencies comparable to other organic solution-processed materials, the low charge carrier mobility in CQD systems remains a major limiting factor. In this section, we will introduce the detailed properties of CQDs and why they have such a low charge carrier mobility. The practical problems we will address in this thesis will follow.

This chapter is written partially based on the published paper: Sangjin Lee, David Zhitomirsky, and Jeffrey, C. Grossman. Manipulating Electronic Energy Disorder in Colloidal Quantum Dot Solids for Enhanced Charge Carrier Transport. *Adv. Func. Mat.*, **26**:1154-1562, 2016

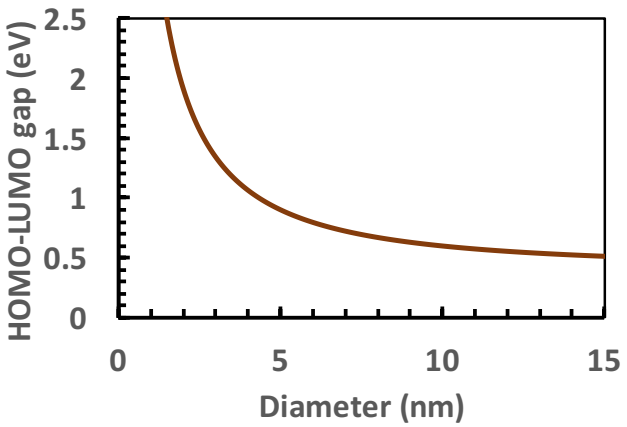

Figure 1-1: The HOMO-LUMO gaps of CQDs increase as their sizes decrease due to the quantum confinement effect. Fitted relation between CQD diameter and the HOMO-LUMO gaps desribed in [1] were used.

1.1 Colloidal Quantum Dots

Colloidal quantum dots (CQDs) are zero-dimensional semiconductor materials that show strong quantum confinement effects. [23] When a electron is excited into conduction bands, it leaves a positive charge (hole) then they make an electron-hole pair, an exciton. An exciton Bohr radius defines a size of the electron-hole pair in the similar logic with a distance between an electron and a proton in a hydrogen atom. When a size of materials becomes smaller than the exciton Bohr radius, electronic and optical properties of the materials are significantly affected by their size. Because of the size-dependent unique optical and electrical properties of CQDs, they have recently been investigated as materials for next-generation optoelectronic devices, where the fact that they provide extremely high tunability in their optical and electronic properties presents an exciting opportunity. Specifically, control over the CQD energy gap, relative energy levels, and optical absorption, combined with their low-temperature solution processability and high stability makes them appealing as candidate materials for the solar cell active layer.

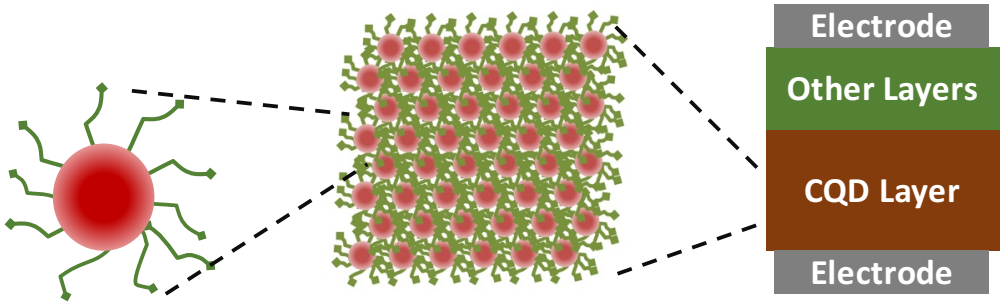

Figure 1-2: A CQD structure: semiconductor cores and ligands attached to the cores (left). CQDs are used as a form of layers in the optoelectronic devices (right).

The energy gap between the highest occupied molecular orbital (HOMO) and the lowest unoccupied molecular orbital (LUMO) of CQDs is determined by their size when the radius of the CQD is smaller than the bulk exciton Bohr radius. Therefore, as shown in Figure 1-1, [1] one can tune the optical properties of CQDs by simply changing their size, which is extremely powerful for designing tailored optical absorption in solar cells, especially in the case of multi-junction tandem structures. [10, 24] Furthermore, in nearly all large-scale processing approaches to CQD layers, ligand molecules used during the synthesis to control growth, will remain attached to the surface of the CQD even after deposited as a layer in a film (see Figure 1-2). While these ligands play critical roles in stabilizing the deposition process and in passivating the surface trap states, they can shift the CQDs energy levels considerably. [17] For example, as reported in Ref. [25], where the scanning tunneling spectroscopy were used to measure the density of states of CQDs with different ligands, simple ligand exchange from trioctylphosphine ligands to aniline ligands, changes the band levels of the CQDs by $\sim 0.3eV$, which is larger than desirable in order to have good control over charge transport at interfaces between CQD layers and adjacent functional layers

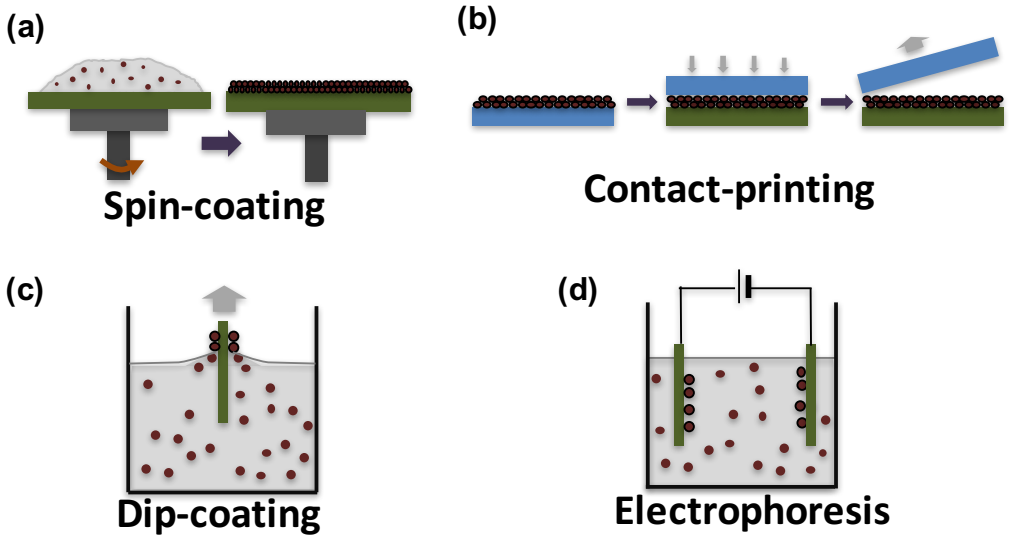

Figure 1-3: Common CQD solid deposition methods: (a) spin-coating, (b) contact(or transfer) printing, (c) dip-coating, and (d) electrophoresis.

in the solar cells. In lead sulfide (PbS) CQDs, which is most commonly used CQD materials for solar cells, up to 0.9eV energy level shifts were recently observed from ultraviolet photoelectron spectroscopy. [26]

In addition to the potential advantages of optical and electronic tunability, CQDs also provide advantages in solar cell device fabrication. Since CQDs are synthesized via solution processing, it is possible to apply wet-processes in the manufacturing of the solar cells, such as spin-coating, [13,27] dip-coating, [28] contact printing, [29,30] and electrophoresis [31] as shown in Figure 1-3. These solution-based processes are not only cheaper than vacuum-based device fabrication, but effective for building complex geometries. Moreover, CQD-based solar cells can show a high degree of robustness in air that is major challenge in polymer-based and perovskite solar cells, since the air-sensitivity of CQDs can be decreased using strongly bound ligands without significant degradation in optical properties [32] and solar cell performances. [15] This robustness enables the potential for encapsulation-free solar cells based on CQD layers, which would be favorable for further cost-reduction.

1.2 CQD based solar cells

CQD based solar cells have been intensively studied and developed since the mid 2000s. Despite such a relatively short history, the best performance of CQD-based solar cells has already surpassed 10% in power conversion efficiently (PCE). [33] Among CQDs used for solar cells, PbS has been investigated actively because of its broadband optical response; the optical spectra of PbS CQDs can covers a broad range of solar light spectrum from a collection of different sizes, including far-infrared, especially when compared with leading absorber materials in organic (P3HT) [34] and inorganic (Si) [35] solar cells which only cover a much smaller part of the visible spectrum.

Although the PCE of CQD based solar cells has shown remarkable improvement for last 10 years (from 1.3% [36] to the current 10% [33]), this value is still to low for CQDs to be appealing in commercial applications. The dominant discrepancy between CQD solar cells being able to take full advantage of the major benefits described above, and the still-low device performance achieved thus far, can be attributed to the low carrier mobility in CQD active layers. The reported charge carrier mobility in PbS CQDs for both electrons and holes covers a broad range, from 10^{-4} to $10^{-2} cm^2/(V \cdot s)$, [12,14,20] much smaller than that of other conductive materials (see Table 1.1). The reason for the low charge carrier mobility in CQD solids is their slow transport kinetics: hopping transport.

Not only does the low charge carrier mobility degrade the charge extraction ability in the CQD solar cells, but it also limits the thickness of the light absorption layer. A diffusion length of charge carriers can be determined from mobility. For example, if mobility become lower, the diffusion length decreases. If light absorption layers in solar cells are thicker than the charge diffusion lengths, charges will be recombined before they reach electrodes where they are collected as currents, degrading solar cell performance. The reported CQD solar cells still have thin CQD layers about 200nm, [15, 33] which is not sufficient to fully absorb sunlight; in fact, more than

Table 1.1: Charge Carrier Mobility of Conductive Materials ($cm^2/(V \cdot s)$)

Materials	Electron Mobility	Hole Mobility
Si [38]	$\sim 2\times10^3$	$\sim 5\times10^2$
GaAs [38]	$\sim 7\times10^3$	$\sim 4\times10^2$
P3HT [39]	$\sim 1\times10^{-2}$	–
PbS (bulk) [40, 41]	7×10^2	2.2∼12.8
PbS (CQD) [12, 14, 20]	$1.6\times10^{-4}\sim 4\times10^{-2}$	1.5×10^{-3}
CdSe (bulk) [42]	7.2×10^2	75
CdSe (CQD) [43, 44]	$3\times10^{-2}\sim 16$	–

1000nm is required. [37]

1.2.1 Principal of operation

The best performance in CQD based solar cells was achieved using a heterojunction architecture. [33] Figure 1-4 shows the energy diagram of the heterojunction PbS CQD solar cells with a ZnO electron transport layer (ETL). When CQD layers absorb sun-light, electron-hole pairs are generated. The electron-hole pairs either make the charge carriers, electrons and holes, or diffuse in a form of bound electron-hole (excitons). While electrons transfer into the electron transport layer, holes are collected in the opposite electrode. Exciton diffusions and dissociation processes can also happen; in this case the dissociation mainly happens at the heterojunction interface. Architecture of solar cells and their photovoltaic performance significantly depend on how quickly the dissociation process can occur. In the case of solar cells based on the organic materials, for example, excitons are dissociated mostly at the heterojunction due to the strong exciton binding energy, leading to the limitation on the absorption layer thickness (under the exciton diffusion lengths).

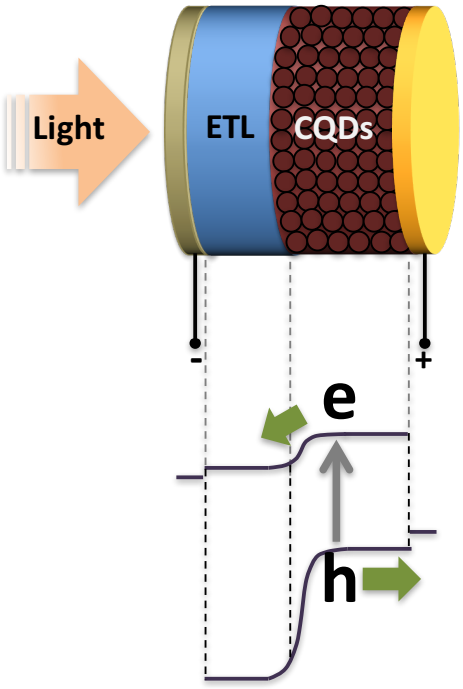

Figure 1-4: A schematic of heterojunction solar cells. The generated charges from the light absorption transfers to opposite directions. While the heterojunction can block the hole transfer and also accelerate the exciton dissociation, electrons transfer to the electron transport layer (ETL).

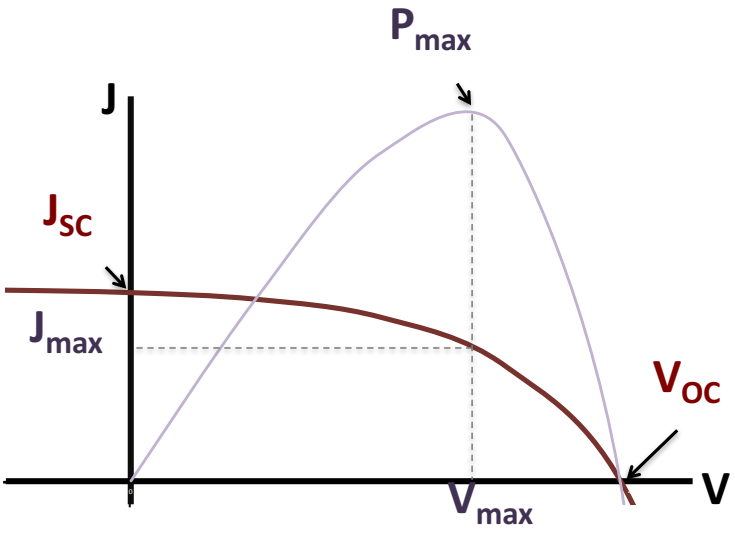

Figure 1-5: A typical J-V curve of solar cells; the red line indicate the J-V curve where the short-circuit current (J_{SC}) and the open-circuit voltage (V_{OC}) are marked. The violet line shows the power generated from the J-V curves; J_{max} and V_{max} indicate the current density and the voltages when the maximum power can be achieved.

The efficiency of solar cells is estimated based on how much power they can produce under the solar light; in fact, simple measurements of electric current at applied bias under illumination can provide such information. A typical current vs. voltage (J-V) curve of solar cells is given in Figure 1-5. The short-circuit current marked as J_{SC} indicates how effective the generated charges can be extracted at the electrodes while the open-circuit voltages marked as V_{OC} defines the maximum differences in chemical potentials of electrons and holes. The power conversion efficiency (PCE) is measured at the maximum power point using the relation:

$$\text{P.C.E} = \frac{J_{SC} \times V_{OC} \times FF}{P_0} \tag{1.1}$$

where FF is the fill factor defined by the ratio of the maximum operating power to the theoretical maximum power, $J_{SC} \times V_{OC}$, and P_0 is the incident solar energy per second.

The generated charges transfer according to the built-in potentials in the short-circuit

case and the net current becomes zero at the open-circuit state where the energy gap between quasi Fermi levels (chemical potentials of electrons and holes) limits the V_{OC}. Large generation rates and high doping levels can increase the V_{OC} by increasing the energy gap, whereas the high charge carrier mobility and the slow recombination of electron-hole pairs are required to enhance the J_{SC}.

1.3 Objectives

1.3.1 Design of CQD solids

Since CQD solids consist of individual CQDs which may have dispersion in their material properties such as sizes, ligand coverages, stoichiometry, and/or shapes, the optical and electrical behavior of CQD solids is measured as an ensemble of those individual properties. Furthermore, the randomly close-packed CQD arrangements in commonly used CQD solids place the localized energy states in a range of positions, causing the inhomogeneity in the interactions among CQDs. In addition to the slow kinetics in charge hopping transport, those disorders in CQD solids can disrupt the transfer of the charges, reducing the charge carrier mobility. In particular, the size-dispersion in CQDs prepared from solution-based processes can change both the energetic structures and the positions, which may alter charge transport behaviors. As shown in Figure 1-6, charge transport in CQD solids with size-dispersion completely differs from that in monodisperse CQD solids. In other words, design of the architecture and morphology of CQD solids can play a critical role in controlling the charge carrier mobility and in enhancing the device performances.

1.3.2 Flow of thesis

In this thesis, we analyze the charge transport in CQD solids in terms of their design factors, such as polydispersity and periodicity, using a hopping transport code we have developed from scratch. After we introduce the details of the computational

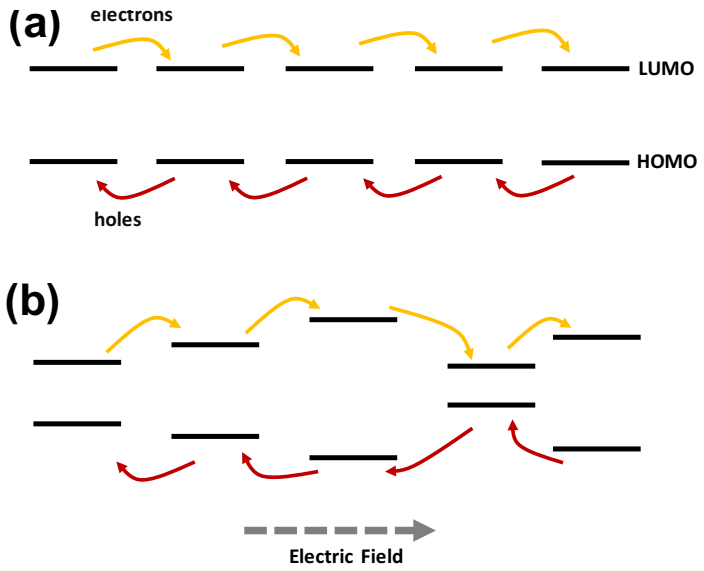

Figure 1-6: Charge carrier transport in (a) monodisperse and (b) polydisperse CQD solids. Electrons (yellow) and holes (red) transfer in opposite directions with respect to applied electric field. The charge transport rates become dissonant when there are inhomogeneities in inter-CQD distance and the electronic energy structures, which leads to slower charge carrier transport.

methods in Chapter 2, out results related to the impact of size-dispersion on charge carrier mobility and the photovoltaic performance will be presented in Chapter 3. In Chapter 4, we suggest design rules and strategies for higher charge carrier mobility in CQD solids, combined with predictions of enhanced photovoltaic performances from such strategies. In Chapter 5, we extend the CQD design strategies to further ideas involving the use of binary CQD solids, which we expect to increase optical absorption and charge transport.

Chapter 2

Methods

While a wide range of theoretical approaches have been employed to understand charge transport phenomena in CQD solids, systematic studies related to the impact of CQD designs in terms of their size have been lacking. This is not only because there is no effective method to trace the individual charge transport rates between CQD pairs, but also because experimental controls on CQD sizes are still extremely cumbersome. Therefore, computational studies of the behavior of charge carriers are essential in order to better understand the transport properties of CQD solids. Moreover, for a complicated system such as a CQD film with inhomogeneity, in which a number of different processes can occur simultaneously, computational approaches provide the ability to separate the role and impact of each process, providing a much deeper understanding of the overall mechanism.

This chapter is written partially based on the published paper: Sangjin Lee, David Zhitomirsky, and Jeffrey, C. Grossman. Manipulating Electronic Energy Disorder in Colloidal Quantum Dot Solids for Enhanced Charge Carrier Transport. *Adv. Func. Mat.*, **26**:1154-1562, 2016

2.1 Charge Transport in CQD solids

CQD solids have been simulated using bulk semiconductor models for the sake of convenience, using existing measurement methods available for various optoelectronic devices; in fact, the reported charge carrier mobilities of CQD solids were obtained from time-of-flight analysis [14] or field-effect-transistor measurements [3], then the measured mobility is used for describing CQD solids. However, in contrast to bulk semiconductor materials, the electron wavefunctions of each individual CQD are usually localized due to the ligands attached to it and the inter-dot distances, causing completely different charge transport mechanism, specifically hopping transport.

Electron hopping transport has been also studied in other systems with localized energy states such as organic semiconductors [45–47] and molecular junctions. [48–50] In contrast to resonant charge transport with strong wavefunction coupling that can be usually found in bulk semiconductor materials, hopping transport requires the assistance of phonons that activate the electrons as they can jump to other CQDs through the energy barriers in the middle of two separated electron states. [51] A simple form of hopping transport equation was suggested by Miller and Abraham, [52] where an exponential form of thermal activation energy was used to define the assistance from phonons. More detailed theory, including coupling energies (overlap integrals between the wavefunctions of a donor and an acceptor) and reorganization energies from the different charge distribution between before and after the transition, was developed later by Marcus. [53] A few studies have built numerical simulation models for predicting transport in a system comprised of localized energy states using mainly two computing methods: direct solution of master-equations [54–58] and kinetic Monte Carlo simulations. [59, 60] The former includes hopping transport rates between the localized energy states and the probability of occupancies (charge density) for the energy states in the equations, which are usually the form of continuity equations for charge carriers, then finds the equilibrium occupancy of charges in each CQD. On the other hand, kinetic Monte Carlo simulations estimate how individual charges behave for each time interval, during which all the processes including recombination, gener-

ation, and transport that occur at randomized probabilities are taken into account. Kinetic Monte Carlo simulations can provide time-dependent information since all the behaviors of charges are recorded but a larger amount of computing resource is required, whereas direct solution of master-equations usually estimate the system in equilibrium within less computation time. While kinetic Monte Carlo can provide accurate simulation as long as all the processes are properly defined since it directly mimics the actual processes, direct solution of master-equations are knowns to be comparable to kinetic Monte Carlo as long as the processes involved are defined in the same manner and the short-term Coulomb interactions are negligible. [61]

2.2 Theoretical background

In order to compute charge transport in CQD solids, we adopt an approach based on the direct solution of master-equations since 1) handling large amounts of samples (more than 5,000 samples) which is required to statistically analyze the inhomogeneity such as polydispersity, demands very large computing resources and calls for short simulation times, [62] 2) thin CQD film thickness along the electric fields may not guarantee enough numbers of states to equilibrate the overall charge transfer in the kinetic Monte Carlo, and 3) describing the charge transport rates between CQDs and electrodes (or bulk semiconductors) becomes easier in the method with direct solution of master-equations; see 2.2.3 for the details.

2.2.1 Charge hopping transport

In order to construct the equations to solve, hopping transport rates between two CQDs have to be defined. Based on the Miller-Abraham hopping equation, [52] the charge transport rate from a donor CQD to an acceptor CQD is defined:

$$r_{D\to A} = N_D V_A H_f \exp\left(-\frac{d}{\alpha_D} - \frac{d}{\alpha_A} - \frac{\Delta E_{D\to A} + |\Delta E_{D\to A}|}{2kT}\right) \tag{2.1}$$

where $r_{D\to A}$ is the hopping transport rate from a donor to an acceptor, H_f is the

hopping frequency, N_D is the number of charges in the donor CQD, V_A is the ratio of empty states for the charge in the acceptor CQD, α_D and α_A represent the localization lengths of donor and acceptor CQDs, respectively, which is set to be comparable to their radii, [63] d is the center-to-center distance between acceptor and donor CQDs, and $\Delta E_{D\to A}$ is the energy difference when the charge transports from the donor to the acceptor. While the localization lengths can vary between CQDs, these changes can be absorbed into the hopping frequency coefficient, H_f, because we assume no enhancement or degradation of interactions in specific CQD pairs, or between a CQD and ligands, exists. This model implies that the charges need thermal activation in order to tunnel through the distance d from lower energy levels to higher energy levels; no extra energy is required to hop from higher energy levels to lower energy levels, leading to a negative $\Delta E_{D\to A}$ and zero thermal activation energy. Note that the charge hopping transport defined by this equations is not limited to neighboring CQD pairs, employing the variable-range-hopping (VRH) mechanism [63, 64] where charge can jump to distant states with lower energy barriers rather than a nearest site with higher energy barriers.

2.2.2 Equations

Figure 2-1 shows an example of the CQD solid unit cell. For all CQDs in the simulation unit cell, our hopping transport simulations solve for equilibrium in the charge continuity equations:

$$\frac{dN}{dt} = G_{ext} - U_{net} + R_{e,in} - R_{e,out} \tag{2.2}$$

$$\frac{dP}{dt} = G_{ext} - U_{net} + R_{h,in} - R_{h,out} \tag{2.3}$$

where $N(P)$ is the number of electrons (holes) in each CQD, G_{ext} is the external generation rate, U_{net} is the net recombination rate, $R_{e,in}(R_{h,in})$ is the incoming rate of electrons (holes) from nearby CQDs within a predefined cut-off distance, and $R_{e,out}(R_{h,out})$ is the outgoing rate of electrons (holes) into the nearby CQDs within

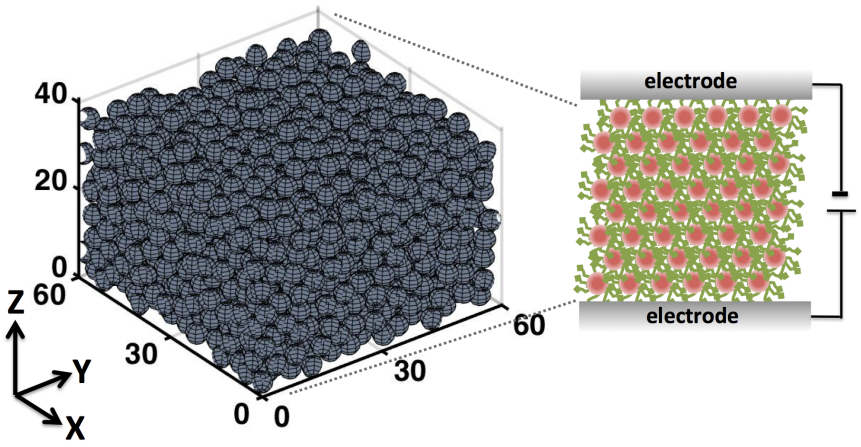

Figure 2-1: An example of CQD film unit cell for a hopping transport simulation (left); two electrodes are set at the top and bottom of the unit cell (right) and the electric fields are applied in the $+z$-direction.

the same pre-defined cut-off distance; charge transport complies with the VRH mechanism, where transport is not limited to the nearest hopping sites, especially for the highly disordered cases. Periodic boundary conditions are employed for the $x-$ and $y-$directions (see Figure 2-1). Each CQD-to-CQD charge transport rate was defined based on equation 2.1.

In addition, electric potentials of the CQDs, determining the shift of energy levels, are estimated based on:

$$\phi = \int_{z_{max}}^{z_{CQD}} \vec{E}(z)dz \tag{2.4}$$

where z_{CQD} is the z-coordinate of the CQD, z_{max} is the maximum z-coordinate of the CQD simulation unit cell (the position of ground electrodes), and $\vec{E}(z)$ is the electric field estimated at each z point with the same $x-$ and $y-$coordinates as the CQD, using all other CQDs' net charge and the applied electric field.

2.2.3 Boundary conditions

While periodic boundary conditions work horizontally ($x-$ and $y-$directions), additional boundary conditions at $z = 0$ and $z = z_{max}$ at the positions of the electrodes are required; since most CQD-based optoelectronic devices usually involve CQD solids as a thin film, periodic boundary conditions at these edges cannot model the actual device working. Rather, charge flows at those boundaries should be estimated with all transport rates from and to the nearby CQDs taken into account. Although there are mainly two simple types of boundary conditions widely used solely or together for charge transport simulations [65,66] (Neumann conditions with fixed flows or Dirichlet boundary conditions with fixed charge densities), neither of these conditions can be incorporated easily into our simulation because 1) the current density at the electrodes should be estimated instead of being fixed, 2) the information on the effective number of charge at the electrode is lacking, and 3) an accurate behavior of individual charge transfer between electrode and CQDs is difficult to obtain either experimentally or theoretically. Therefore, we set the boundary conditions at the electrodes by comparing the equilibrium energy levels as described in Figure 2-2.

The chemical potential of electrons, for example, can be determined in CQDs near the electrodes using their electron occupancies, which is shown as dashed line A in Figure 2-2(a). When the Fermi level of the metal electrodes is at the same level with the electron chemical potential of the CQD, the net electron transport becomes zero, meaning equilibrium. In the case where the chemical potential of electrons in the CQD lies in unbalanced positions with the Fermi level of the metal electrode, such as the dashed line B, a larger amount of electron flow occurs into the CQD (L) than from the CQD (R), giving an overall net electron flux into the CQD. In our simulation, we calculate the electron flow from the electrode (L), based on the electron transport rate from the CQD to the electrode using the number of electrons assuming the electron chemical potential is placed in balanced with the electrodes (the dashed line C). While this method does not require knowledge of the detailed behavior of charges and the transport probability, which is essential for kinetic Monte Carlo sim-

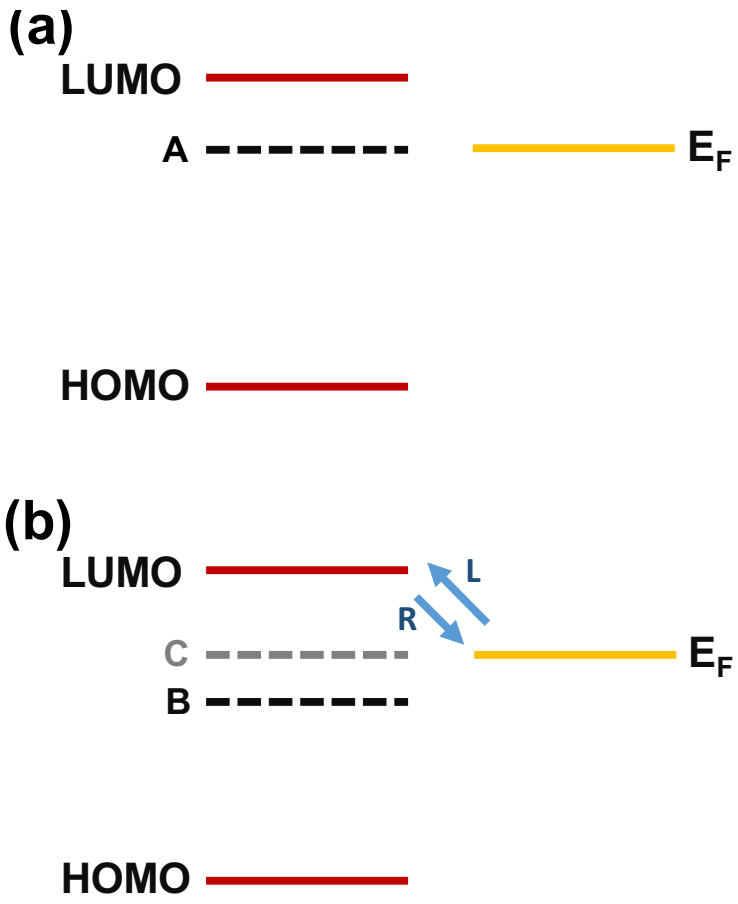

Figure 2-2: Boundary conditions in the hopping transport code: (a) at equilibrium, the chemical potential of the charge (electrons in this case) lies in balance with the Fermi level of the electrode, and (b) the electron transport rates from the electrode to the CQD LUMO level (L) become larger than the rate in the opposite way (R) until the net charge transfer become zero. The larger rate (L) increases the number of electrons in the CQD LUMO level, pushing the chemical potential from B to C which is in balance with the Fermi level of the electrode. The transport rate (L) is defined as the balanced transport rate with the charge transport rate from the CQD LUMO level to the electrode assuming the electron chemical potential is in the level C. This definition does not require the detailed information in charge density in the electrodes and in the form of transport rates between the CQD and the electrodes.

ulations, the current density into/from the CQD solids can be easily estimated using the number of charges and the electric potentials of the CQDs, which are variables we solve for in our approach. Note that in the case of Figure 2-2, this method allows the incoming electrons from the electrodes (L) to keep flowing until the number of electrons in the CQD reaches the balanced electric potentials.

2.3 Flow of simulations

Figure 2-3 shows the overall flow of our CQD charge transport simulation approach. We input each CQD's information including a coordinate, energy levels and, if necessary, a doping level. Doping levels of CQDs are used for solar cell simulations where the number of ionized dopants are directly defined for each CQD. The external generation rates are also able to be included when we simulate the CQD solar cells device performance. A multivariable Newton method [67] is adopted to solve the equations 2.2, 2.3, and 2.4 under a given external electric field. For each CQD, there are three variables (N_i, P_i, and ϕ_i) updated at each step using Jacobian Matrix:

$$\begin{pmatrix} \Delta N_1 \\ \Delta P_1 \\ \Delta \phi_1 \\ \Delta N_2 \\ \Delta P_2 \\ \Delta \phi_2 \\ \vdots \\ \vdots \\ \vdots \end{pmatrix} = \begin{pmatrix} \frac{\partial F_{N_1}}{\partial N_1} & \frac{\partial F_{N_1}}{\partial P_1} & \frac{\partial F_{N_1}}{\partial \phi_1} & \frac{\partial F_{N_1}}{\partial N_2} & \frac{\partial F_{N_1}}{\partial P_2} & \frac{\partial F_{N_1}}{\partial \phi_2} & & & \\ \frac{\partial F_{P_1}}{\partial N_1} & \frac{\partial F_{P_1}}{\partial P_1} & \frac{\partial F_{P_1}}{\partial \phi_1} & \frac{\partial F_{P_1}}{\partial N_2} & \frac{\partial F_{P_1}}{\partial P_2} & \frac{\partial F_{P_1}}{\partial \phi_2} & \cdots & \cdots & \cdots \\ \frac{\partial F_{\phi_1}}{\partial N_1} & \frac{\partial F_{\phi_1}}{\partial P_1} & \frac{\partial F_{\phi_1}}{\partial \phi_1} & \frac{\partial F_{\phi_1}}{\partial N_2} & \frac{\partial F_{\phi_1}}{\partial P_2} & \frac{\partial F_{\phi_1}}{\partial \phi_2} & & & \\ \frac{\partial F_{N_2}}{\partial N_1} & \frac{\partial F_{N_2}}{\partial P_1} & \frac{\partial F_{N_2}}{\partial \phi_1} & \frac{\partial F_{N_2}}{\partial N_2} & \frac{\partial F_{N_2}}{\partial P_2} & \frac{\partial F_{N_2}}{\partial \phi_2} & & & \\ \frac{\partial F_{P_2}}{\partial N_1} & \frac{\partial F_{P_2}}{\partial P_1} & \frac{\partial F_{P_2}}{\partial \phi_1} & \frac{\partial F_{P_2}}{\partial N_2} & \frac{\partial F_{P_2}}{\partial P_2} & \frac{\partial F_{P_2}}{\partial \phi_2} & \cdots & \cdots & \cdots \\ \frac{\partial F_{\phi_2}}{\partial N_1} & \frac{\partial F_{\phi_2}}{\partial P_1} & \frac{\partial F_{\phi_2}}{\partial \phi_1} & \frac{\partial F_{\phi_2}}{\partial N_2} & \frac{\partial F_{\phi_2}}{\partial P_2} & \frac{\partial F_{\phi_2}}{\partial \phi_2} & & & \\ & \vdots & & & \vdots & & & \ddots & \\ & \vdots & & & \vdots & & & & \\ & \vdots & & & \vdots & & & & \end{pmatrix}^{-1} \begin{pmatrix} F_{N_1} \\ F_{P_1} \\ F_{\phi_1} \\ F_{N_2} \\ F_{P_2} \\ F_{\phi_2} \\ \vdots \\ \vdots \\ \vdots \end{pmatrix} \tag{2.5}$$

where F_{N_i} and F_{P_i} are the right side of the charge continuity equations 2.2 and 2.3, and F_{ϕ_i} is set to zero when they find the equilibrium electric field is found, defined

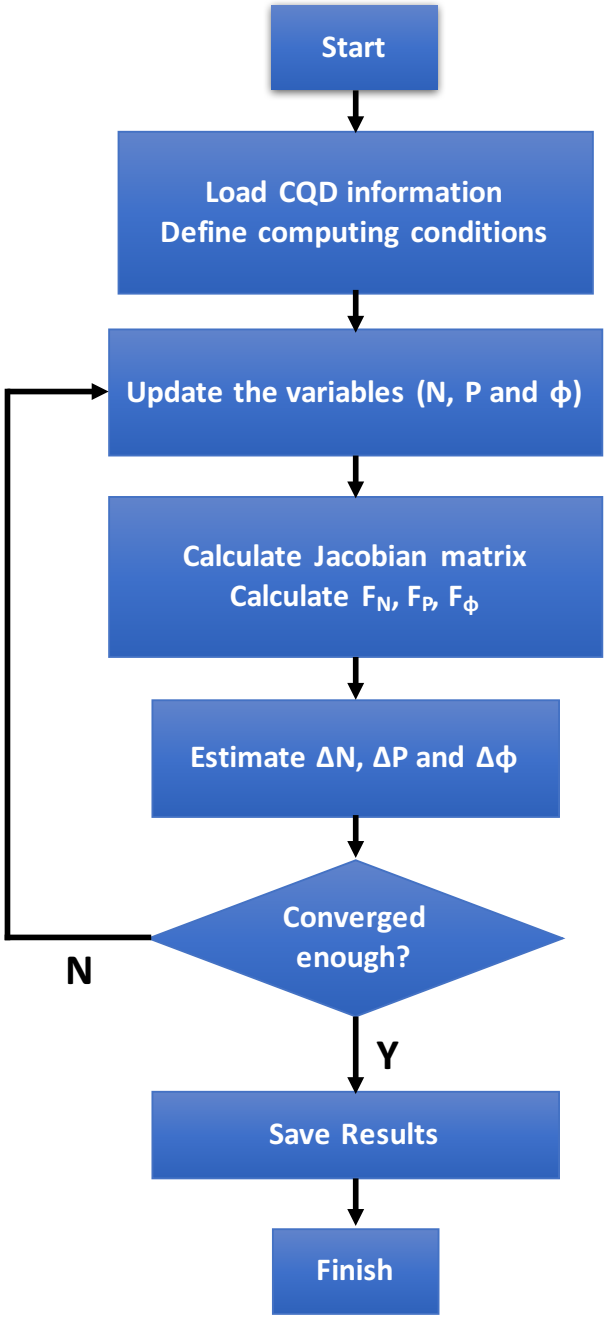

Figure 2-3: The flow chart of the hopping transport simulation code; using the multivariable Newton method, the code computes the number of charges and the electric potential for each CQD in equilibrium based on the loaded CQD information on their positions and the electronic structures.

by equation 2.4;

$$F_{\phi_i} \equiv \phi_i - \phi = \phi_i - \int_{z_{max}}^{z_i} \vec{E}(z)dz \tag{2.6}$$

The computation loop in Figure 2-3 keeps running until the variables and the current density converges under a pre-defined relative tolerance (10^{-8}). In addition to the convergence tests carried out for the unit cell sizes in order to exclude finite size effects from the periodic boundary conditions, the cut-off distance for the hopping transport rates was taken to be long enough to include all possible transport pairs. The computation code includes hybrid parallelizations using both the shared-memory and distributed-memory parallelization. In the shared-memory parallelization, the computing cores (central processing units, CPUs) can access the shared memory quickly but the number of available cores has a limitation from the computer architecture, while the distributed-memory parallelization uses many number of systems, which are easily added to expand computing resource, communicating one another (slower than the shared-memory parallelization) in order to send and receive data computed separately in individual systems. Considering the large amount of computational samples for statistical analysis of the effects of inhomogeneity in CQD systems demanding significant computing resources even if we use the relatively simple direct solution of master-equation method, extensive parallelization is essential for obtaining results within a reasonable time; in fact, the actual computation time was reduced by more than 100 times as shown in Figure 2-4 where the computation time for one step of the computation loop, including Jacobian matrix inversion (gaussian elimination) and integrating on the electric field, with respect to the level of parallelization is plotted.

2.3.1 Major assumptions

We note that the variables in equation 2.1 are time-averaged in the equilibrium of the charge continuity equations (2.2 and 2.3); for example, N_D is allowed to be a non-

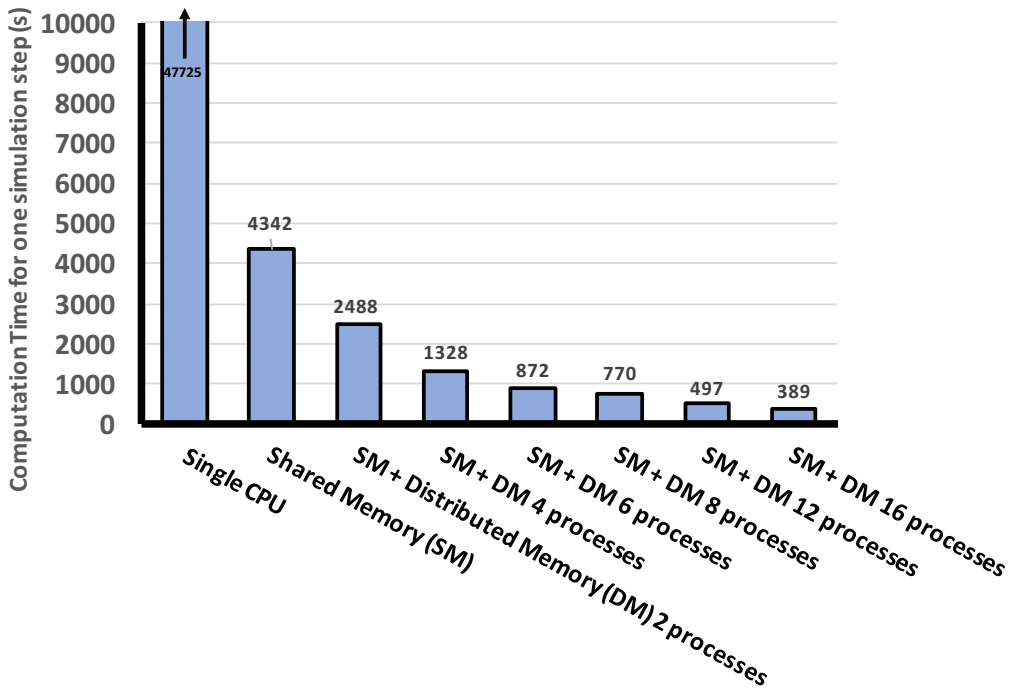

Figure 2-4: Computing times for one step in the loop of the hopping transport code with respect to the level of parallelization. The number of process indicates how many nodes were used for distributed memory (DM) parallelization, where each node run a single process at shared memory (SM) parallelization. A single-core process takes 120 times longer than extensive the hybrid parallelization cases.

integer. Although non-integer numbers for charge can significantly underestimate charge-to-charge interactions such as the Efros-Shklovskii Variable Range Hopping (ES-VRH) at low temperature, ES-VRH is known not to be dominant in the temperature used in out simulations ($300K$); [68, 69]

The localization lengths of CQDs are set to their radii of them under the assumption that the electron wavefunctions are confined inside the CQDs. While there can be some modifications in localization lengths from the local charging energies and electrostatic potential, we assume that such effects are negligible because 1) the average number of charges for CQDs in equilibrium were found to be very small, and 2) applied electric fields from computing the charge carrier mobility were found to be much higher than the local electric fields induced by those small numbers of charges, adding negligible gradients in the electric potentials of CQDs in the applied electric field direction, which presumably leads to no significant changes in overlap integrals of the wavefunctions in the electric field directions despite the asymmetry in the individual wavefunction. Recent reports showed that the localization lengths may change dramatically as a function of doping of the CQDs but the critical doping level is significantly higher (more than 10 electrons or holes per CQD) than the value we used in our simulation of photovoltaic performance estimation (10^{-4} hole per CQD). [70]

We did not include charging effect in estimating charge hopping rates. While the exact charging energies are quite difficult to address in our simulation because of the time-averaged non-integer number of charges, it has been reported that the charging energy usually increased when nanoparticle size decreases. [71] This size-dependent charging energy can actually intensify the site-energy dispersions in the polydisperse CQD films.

We used the HOMO and LUMO levels as effective charge transport paths. Involvement of higher energy levels (for example, the second lowest occupied levels and the second highest unoccupied levels) can increase the charge carrier mobility of CQD films by providing additional states available for charge transfer. However, as shown in Figure 2-5, we confirmed that such effects disappears when the energy difference between the first and second energy levels is larger than 150meV, as is the case for

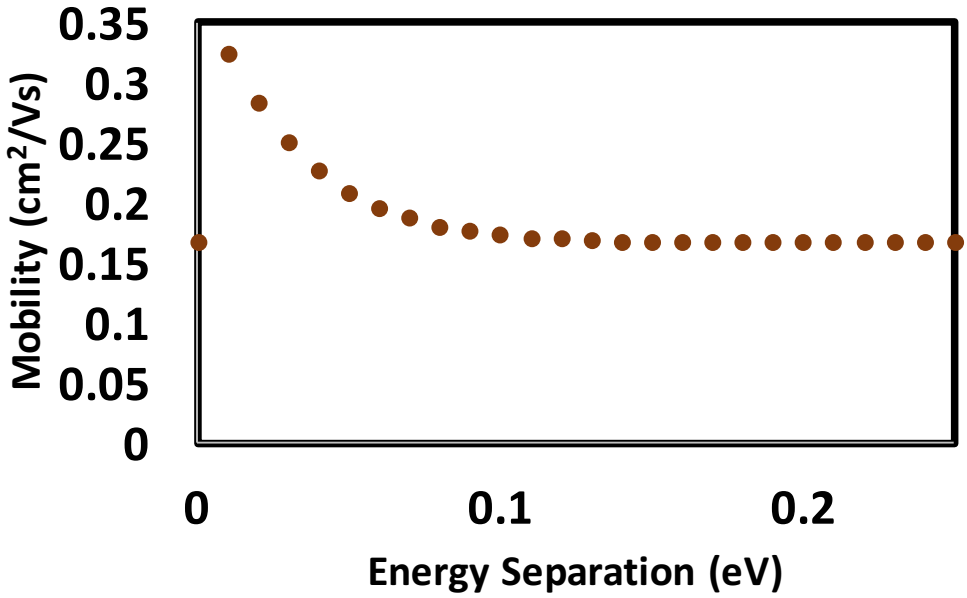

Figure 2-5: Trend in electron mobility when the 2nd lowest unoccupied energy levels are included into the simulation; we confirmed that the second levels can be ignored when the separation between LUMO levels and the 2nd lowest unoccupied energy levels is larger than 0.15eV, where differences from the LUMO-only electron mobility become lower than 0.1%.

the range of PbS CQD sizes we are interested in (under 3nm in radius). [1, 4]

2.4 Validity test

The computed electric transport characteristics of the CQD solids showed trends in good agreement with experimental measurements of the field-dependence of conductance [2] (Figure 2-6(a)), temperature dependence of conductance [2] (Figure 2-6(b)), and exponentially increasing mobility with decreasing ligand length [3] (Figure 2-6(c)). The conductivity and the mobility in these experiments were estimated using FET measurements. While the agreements in trends between our simulation results and the experimental measurement can guarantee that the systems are in the same charge transport regime, the numbers such as current densities, mobility, or conductances, differ from each other because the detailed experiment conditions cannot be taken into account in the simulation; instead, we use the hopping frequency, H_f in

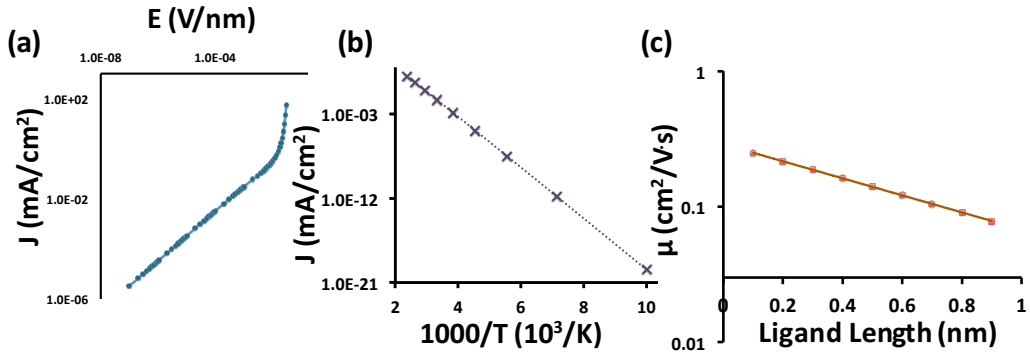

Figure 2-6: Simulation results that show good agreement with the data from experimental measurements: (a) electric field dependency of the current density for closed-packed CQD solids. Current density shows the similar trends to the experimental measurement including ohmic to non-ohmic transitions at the high electric field (Ref [2]), (b)The computed temperature dependency of the current density for close-packed CQD solids in good agreement with experimental trends in Ref [2], and (c) The computed trends in charge carrier mobility with respect to the ligand lengths; exponential increases in charge carrier mobility with decreasing ligand lengths show a good agreement with the measured mobilities in Ref [3].

equation 2.1, which can be relatively tuned with respect to the conditions we want to investigate. While the agreed trends in the field-dependence of conductance confirm that the equation 2.1 simulates the experiment well in terms of how the site energy difference reduces the charge transport, the same trends in temperature dependence of conductance between the simulations and the experiments verify that thermal activation process is well defined in our code and the simulated CQD systems have no strong charge-to-charge interactions. The exponential decay of mobility with increasing ligand lengths, which is also observed from the experiments, supports that overlaps between localized wave functions are well described with the exponential form for the center-to-center distances and the localization lengths in the equation 2.1.

Chapter 3

Polydispersity in CQD solids

Although CQD solids have been widely applied in optoelectronic devices taking advantage of their unique optical properties, as mentioned in Chapter 1 such applications have been limited by the relative low charge carrier mobility of CQD films. Polydispersity introduced to the CQD solids has been believed to significantly degrade the charge transport throughout the film since energetic and spatial disorders cause inhomogeneity in the hopping transport. In this chapter, the impact of this electronic energy disorder originating from the size dispersion of CQDs on the charge carrier mobility in CQD solids will be analyzed. Then, we will show how the CQD solar cells performance is affected by size-dispersion.

This chapter is written partially based on the published paper: Sangjin Lee, David Zhitomirsky, and Jeffrey, C. Grossman. Manipulating Electronic Energy Disorder in Colloidal Quantum Dot Solids for Enhanced Charge Carrier Transport. *Adv. Func. Mat.*, **26**:1154-1562, 2016

3.1 Low Mobility in CQD Solids

As we have already discussed, the relatively low charge carrier mobility (0.0001-0.01$cm^2V^{-1}s^{-1}$) [12, 20, 72] in CQD active layers originates from the fact that the charge carrier transport depends mainly on slow kinetics, namely vis a hopping transport mechanism. [51, 73] A number of studies have explored ways to enhance the carrier mobility in CQD layers, including the use of shorter ligands, [3] reduction of trap density by surface passivation, [74,75] alignment of energy levels with ligands for nearly resonant transport, [76] and induction of band-like transport; [44] in some cases charge carrier mobilities higher than $10cm^2V^{-1}s^{-1}$ have been achieved. [77–80] Size dispersion in as-synthesized CQDs is considered another source of mobility loss and device performance degradation. CQDs synthesized from conventional wet-chemistry processes possess a 5%-15% size dispersion, [3,81,82] causing a corresponding dispersion in the energy gaps between the HOMO and LUMO of the individual CQDs. This inhomogeneity in electronic energy levels can disrupt the charge hopping transport in CQD films and degrade the transport rate significantly. In addition, a sufficiently narrow CQD size dispersion is essential to achieve the periodic super-crystals that have shown dramatic enhancement in carrier mobility in CQD field effect transistors due to the reduced inter-particle spacing and increased exchange coupling from the ligand treatment. [83] The impact of CQD size dispersion on the charge carrier mobility in CQD films is little understood, and apparently contradictory results such as a lack of correlation between polydispersity and carrier mobility [3, 59] versus the high carrier mobility observed using monodisperse CQDs, [83] calls for further investigation into the impact of radius distribution of CQDs on the carrier mobility in CQD films. Furthermore, while recent work showed that CQD solar cell performance was not influenced by polydispersity since a high density of deep trap states degraded the charge transport in CQD active layers regardless of their size dispersion, [84] new concepts involving small ionic ligands and hybrid passivation strategies could successfully inactivate those trap states, [75] motivating the need for detailed studies on the impact of the CQD polydispersity, and for the establishment of design rules for

polydisperse CQD solids.

3.2 Impact of Polydispersity on Charge Carrier Mobility

3.2.1 Preparation of CQD Solids

While a variety of CQD film deposition methods have been employed experimentally such as spin-casting, dip-coating, and electrophoresis, regardless of the technique the deposited films all possess randomly close-packed (RCP) CQD arrangements. [31, 77, 85] Thus, in our calculations we define the positions of CQDs in the RCP arrangement, via molecular dynamics (MD) simulations with spherical particles and a granular potential, mimicking the experimental CQD films deposition process. Figure 3-1 shows a schematic of the CQD solid preparations, where we adopted a two-step process: 1) place CQDs sparsely above the MD simulation box, then 2) start the MD simulation with a granular potential and an additional acceleration to force the particles into the simulation box. As discussed in Chapter 2, periodic boundary conditions are applied in the horizontal directions. The computations were carried out using the LAMMPS packages [86] where the granular potential adopted the Hookean styles described in Refs. [87–89]; the granular potential provides a strong repulsive force between two spheres only when they are overlapped with shorter inter-distances than the sum of their radii. After CQDs lose their energy from collisions, finally, the CQDs find their equilibrium positions as shown in Figure 3-1(c), which are then used in the hopping transport simulation code described in Chapter 2.

3.2.2 CQD solids with size-distribution

Computational samples of CQD films with 0%-15% size dispersions were prepared using MD simulations. Assuming each CQD with 4Å ligand length is a sphere, 1600 radii of CQDs were generated with a normal distribution with standard deviation ranging from 0 to 0.285 nm and an average radius of 1.9 nm. We refer to the bottom

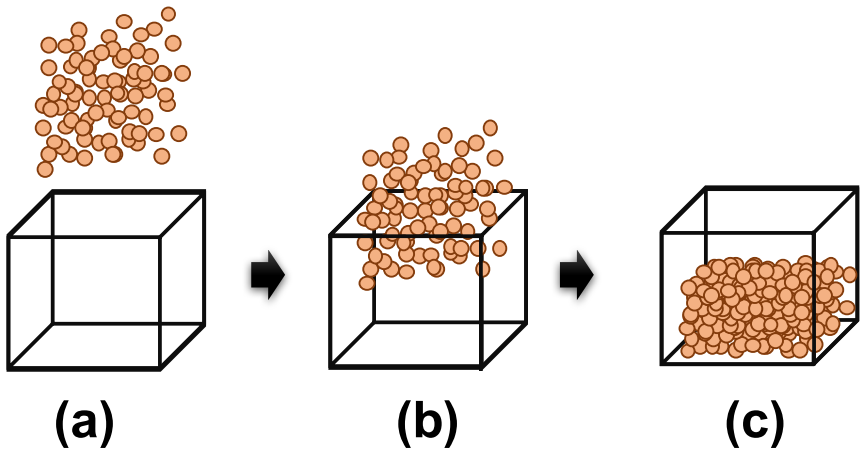

Figure 3-1: A schematic of CQD film preparation for hopping transport simulations: (a) place CQD spheres sparsely above the MD simulation box, then sort them with respect to their size if necessary, (b) start MD simulations under the granular potential among CQD spheres and an additional downward acceleration, and (c) CQD spheres find their equilibrium positions.

of the simulation cell as the xy-plane (60 nm $\times$ 60 nm) located at $z = 0$ and the height of the cell corresponds to the z-axis (Figure 2-1). Generated CQD solids from the procedure described in the previous section have RCP configurations with packing density around 0.605, in good agreement with the reported results on the trend of core to total volume ratio with respect to the inter-CQD distance in the face-centered-cubic-like (FCC-like) amorphous phase. [90]

Next, positions and radii of CQDs were used to model charge transport where HOMO-LUMO gaps were calculated using a relation for lead sulfide (PbS) CQDs suggested by Moreels *et al.* [1], where d is the core diameter, and E_g is the HOMO-LUMO gap.

$$E_g = 0.41 + \frac{1}{0.0252d^2 + 0.283d} \tag{3.1}$$

While the HOMO-LUMO gaps broaden as the CQD size decreases due to the quantum confinement effect, the changes in the individual energy levels are not symmetric. We therefore determined the HOMO and LUMO levels based directly on experimental

results from Hyun *et al.*, [91] where the increases in LUMO levels with decreasing CQD size is larger than the decreases in HOMO levels.

The charge carrier mobility of CQD solids was estimated using the current density at 0.001 Vnm^{-1} electric field, comparable to the electric field inside the depletion layer in conventional CQD solar cells working at the maximum power point [37] or that between sources and drains in CQD field effect transistors, [44] and using the total number of carriers in the layers when all the charge continuity equations become close enough to zero so that the current densities converged to within 10^{-8} of the relative tolerance. Note the charge carrier mobility estimated in this simulation includes contributions from all the charge distribution in the CQD solids and the internal electric field from the charge distribution since it is measured from external variables such as current density at the electrodes and the applied electric field.

3.2.3 Impact of polydispersity on the charge transport

Figure 3-2 shows the trends of electron and hole mobility with increasing CQD size dispersion. 50 different samples were averaged for each size dispersion. Note that a 70% loss in the electron mobility is observed for samples with size dispersion around 10%. On the other hand, the hole mobility shows only a 11% decreases even in the most dispersive (15%) CQD radius distribution cases. This mobility reduction and the differences in electron and hole mobilities can be understood from the relation between spreads in site energy differences and the CQD size dispersion.

Figure 3-3 shows the increases in the standard deviations in neighboring site energy differences ΔE between hopping pairs for all CQDs as the size dispersion broadens. Since the hopping transport equation 2.1 includes the energy difference terms inside the exponent, the variance in the neighboring site energy differences distracts the charge hopping transports into neighboring CQDs in terms of their directions and rates. The smaller reduction in the hole mobility can be attributed to the small increases in site energy deviation even for a large CQD size dispersion. We further tested this model to investigate the trends of charge carrier mobility in additional tem-

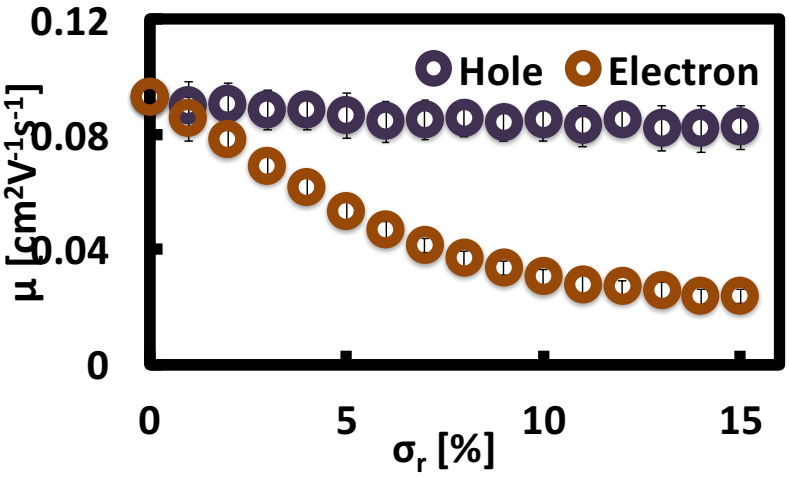

Figure 3-2: Charge carrier mobility of CQD solids with respect to the polydispersity; the large drops are observed in electron mobility at 10-15% polydispersity while the hole mobility did not show significant reduction.

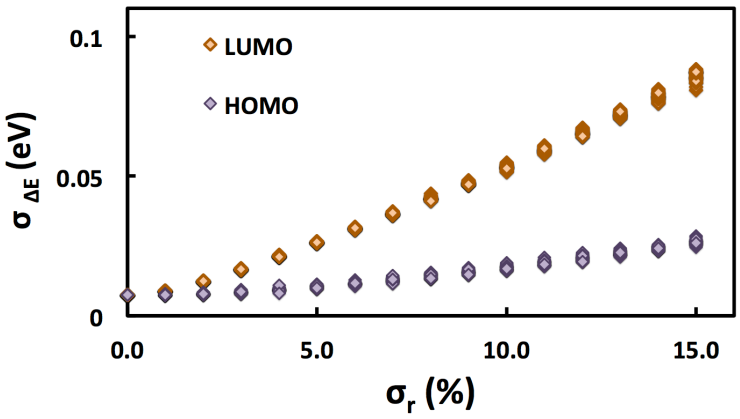

Figure 3-3: Standard deviations of site energy differences for each sample with respect to the size-dispersion in CQD ensemble; 50 samples were tested for each CQD size-dispersion.

Table 3.1: Electron mobility drops at 10% polydisperse CQD solids.

Temperature (K)	Mean Radius (nm)	Ligand Length (nm)	Electron mobility drops at 10% polydispersity
200	1.9	0.4	87.7%
250	1.9	0.4	77.3%
350	1.9	0.4	57.1%
300	**1.7**	0.4	72.0%
300	**2.1**	0.4	61.8%
300	**2.3**	0.4	54.3%
300	1.9	**0.2**	62.0%
300	1.9	**0.6**	70.5%
300	1.9	**0.8**	73.4%

perature and mean size parameters; more than 54% of the electron mobility drops were observed from a wide variety of samples shown in Table 3.1.

The mobility drops become significant at low temperature, where not enough thermal energy is available for charges to overcome the energy barrier in polydisperse CQD solids. VRH can provide other transport paths but the transport rates become significantly low due to the increased hopping distance. An increased mean radius makes the dispersion of site energy differences moderate, leading to less impact of polydispersity on the mobility drops. Longer ligands exponentially decrease the charge hopping transport rates in our model as expected from the equation 2.1, where d increases with longer ligands. Shorter ligands may provide more states available for charges to hop in shorter distance in the VRH regime, lowering the impact of

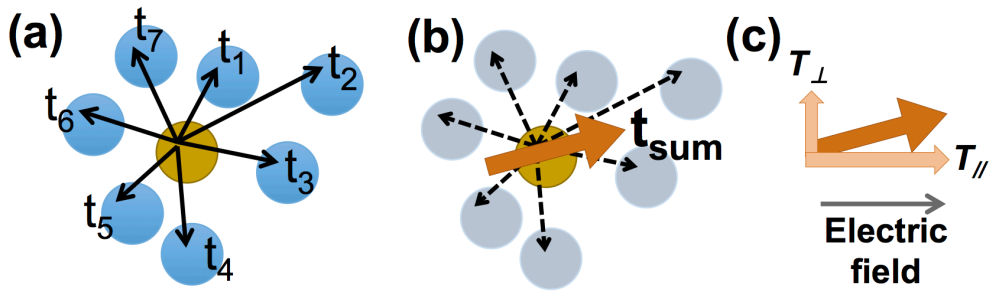

Figure 3-4: Hopping transport rate vector analysis: (a) for each CQD, all the hoping transport pairs illustrated as vectors with hopping rates and hopping directions, (b) transport rate through each CQD from summation of those vectors, and (c) dividing it into two directions with respect to the electric field.

polydispersity on the mobility drops.

In order to further analyze the impact of these divergences on hopping transport, we adopted *hopping rate vectors* that represent the intensity and directions of each transport rate between all the transport pairs. The intensity of these vectors is defined by Equation 2.1 and the directions are calculated using the positions of the CQDs in each transport pair (Figure 3-4(a)). Adding all these transport vectors in each CQD, we obtained the overall transport rate and direction through each CQD ($\vec{t}_{sum}$ in Figure 3-4(b)), then evaluated how much of this transport rate differs from the electric field direction; we defined $T_{//}$ (parallel to the electric field) and $T_{\perp}$ (perpendicular to the

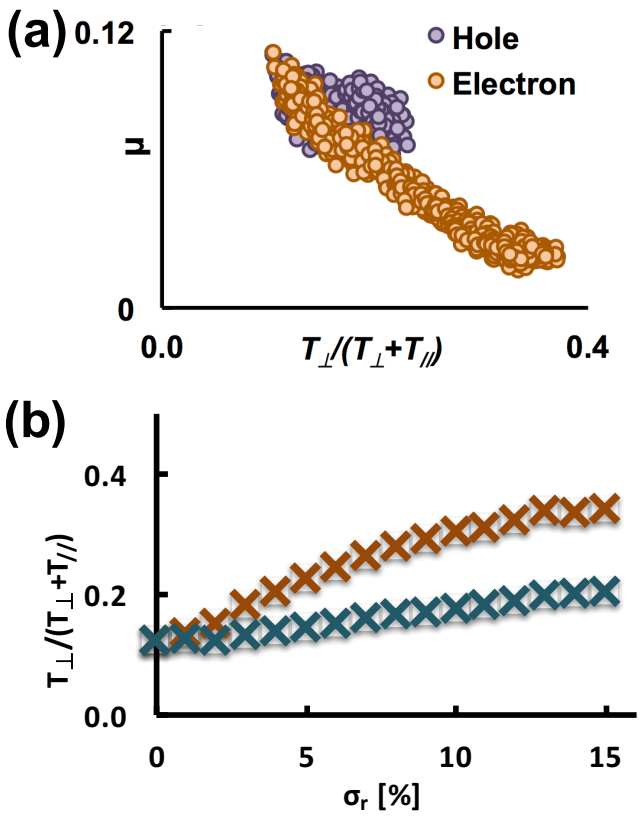

Figure 3-5: Hopping transport rate vector analysis on the polydisperse CQD solid samples: (a) charge carrier mobility in CQD solids decreases as the portion of transport along the electric field decreases, and (b) the portions of charge transport rate perpendicular to the electric field increases as size dispersion increases.

electric field) as:

$$\begin{aligned} T_{//} &\equiv |\vec{t}_{sum} \cdot \hat{e}| \\ T_{\perp} &\equiv |\vec{t}_{sum} - (\vec{t}_{sum} \cdot \hat{e})\hat{e}| \\ \hat{e} &= \vec{E}/|\vec{E}| \end{aligned}$$

where $\vec{E}$ is the electric field. Since $T_{\perp}$ indicates how much of the total transport in each CQD differs from the electric field direction, $T_{\perp}/(T_{\perp} + T_{//})$ from all the CQDs in each solid can be used to evaluate its charge transport capability along the electric field. The trends of $T_{\perp}/(T_{\perp} + T_{//})$ are shown in Figure 3-5. The plots imply that charge carrier mobility in CQD films degrades with increased size dispersion due to the inhomogeneity in energy level differences between hopping transport pairs which in turn alters the charge transport from the electric field direction, indicating that a larger portion of hopping transport rates in the electric field direction boosts the overall charge carrier mobility. This analysis of the mobility drops in polydisperse CQD films suggests that, in addition to a reduction in the site energy deviations, an increase in electric-field-oriented charge transfer will also serve as desirable design rules for higher mobility CQD films.

3.2.4 Degradation in Photovoltaic Performances

We used the same set of CQD unit cells for calculations of photovoltaic performance. CQDs are p-doped with 10^{-4} positive charges per each CQD, leading to Fermi levels at about 0.3 eV above the HOMO levels. Heterojunction photovoltaic cells were modeled with hole blocking boundary conditions replacing the ohmic ground electrode at the maximum z coordinate of the unit cells. Optical generation terms in the charge continuity equations were set to $4{\times}10^{3}$ for all CQDs, which is set to high enough since we used thiner CQD light absorption layers than experiments for short-computation time. The energy levels of the conduction band minimum (CBM) and the valence band maximum (VBM) are shown in the inset in Figure 3-6; the hole blocking barrier is set to a lower height than the conventional experimental structures with ZnO or

TiO_2 thin films in order not to make the computations unstable, allowing a small amount of hole diffusion into the blocking layers; it was confirmed that large hole accumulations from large barrier heights observed during the computing steps can prevent the variable from being converged.

The J-V curves for 0-15% polydisperse CQD heterojunction photovoltaic cells are shown in Figure 3-6. Polydispersity in CQD solids largely degrades all of the figures-of-merit: 8% in the short-circuit current, 15% in the open-circuit voltage, 16% in the fill factor, and 34% in the power conversion efficiency (PCE) at a 10% size-dispersion. The large amount of reduction in PCE indicates that if monodisperse CQD solids become available for solar cells, we can achieve about a 15% PCE, which can outperform other wet-processable materials for solar cells, from the current champion CQD solar cell structures (10.6%). [33]

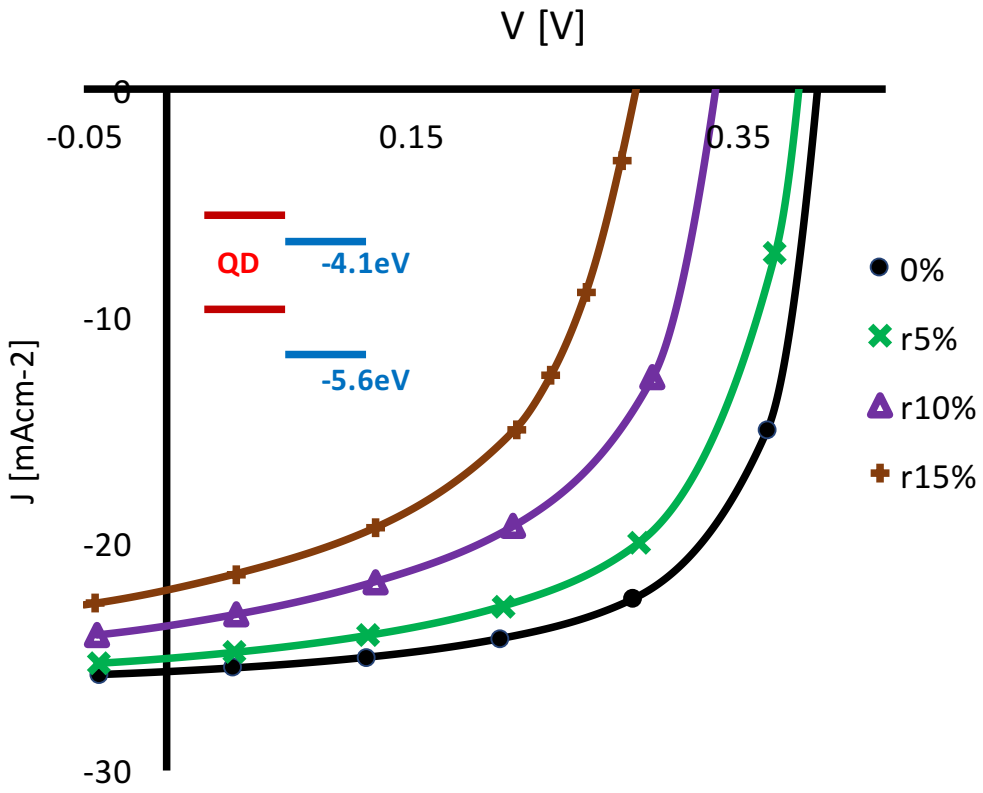

Figure 3-6: Degradations in photovoltaic performance by polydispersity; all the figures-of-merit are reduced including 34% reduction in power conversion efficiency.

Chapter 4

Polydispersity Controls for Enhanced Charge Transport

In the previous chapter, we showed that the size-dispersion in CQD solids significantly reduces the charge carrier mobility, leading to a large degradation in photovoltaic performances. While monodisperse CQD solids could resolve this issue, in this chapter we suggest the alternative ways to mitigate such effect: namely, sorting the polydisperse CQDs. Using the charge transport model we developed, we tested simple re-arrangements of CQDs with respect to their size and analyzed how they provide a new venue for enhanced charge transport.

This chapter is written partially based on the published paper: Sangjin Lee, David Zhitomirsky, and Jeffrey, C. Grossman. Manipulating Electronic Energy Disorder in Colloidal Quantum Dot Solids for Enhanced Charge Carrier Transport. *Adv. Func. Mat.*, **26**:1154-1562, 2016

4.1 Sorting CQD solids

As we showed in the previous chapter, one strategy to maintain the highest charge carrier mobility in CQD solids could involve synthesizing monodisperse CQDs or narrowing the size dispersion from the as-synthesized polydisperse CQDs before depositing into active layers. However, achieving perfectly monodisperse CQDs is currently unrealistic given the hot-injection methods used in CQD synthesis and lack of efficient nanometer scale filtration methods, although recent work reported a $\sim 5\%$ size dispersion; [92] even in this case our calculations show that 40% of the potential electron mobility is lost. Furthermore, several types of CQD systems including III-V composites inherently have difficulties in being prepared with small size dispersion [93] due to their unique synthesis process. [94] Another approach to achieve efficient charge transport in CQD films could be to redesign the CQD configurations within the film even though considerable size dispersion exists in the as-synthesized colloidal CQDs. While computational approaches allow for any distribution of CQDs to be tested, here we adopt ones that may be practically realized, such as a film possessing a gradient of colloidal CQD radii in different directions: vertical (in the electric field) or horizontal (perpendicular to the electric field).

4.2 Size Gradient along the Electric Field

We compared three types of computational unit cells (Figure 4-1) where the effective radii of CQDs have: (1) a random distribution, (2) an ascending order in the $+z$-direction, and (3) a descending order in the $+z$-direction; the $+z$ direction is parallel to the electric field. Examples of radius profiles for CQD locations in each unit cell with 15% size-dispersion are also shown in Figure 4-1(d)(e)(f). The arrangements of CQD radii described above were applied prior to placing the CQDs into the simulation box and starting the MD simulation since artifacts such as unphysical overlapping of neighboring CQDs are possibly introduced into the CQD geometry if the positions of CQDs are exchanged after the MD equilibration. In addition, this pre-deposition

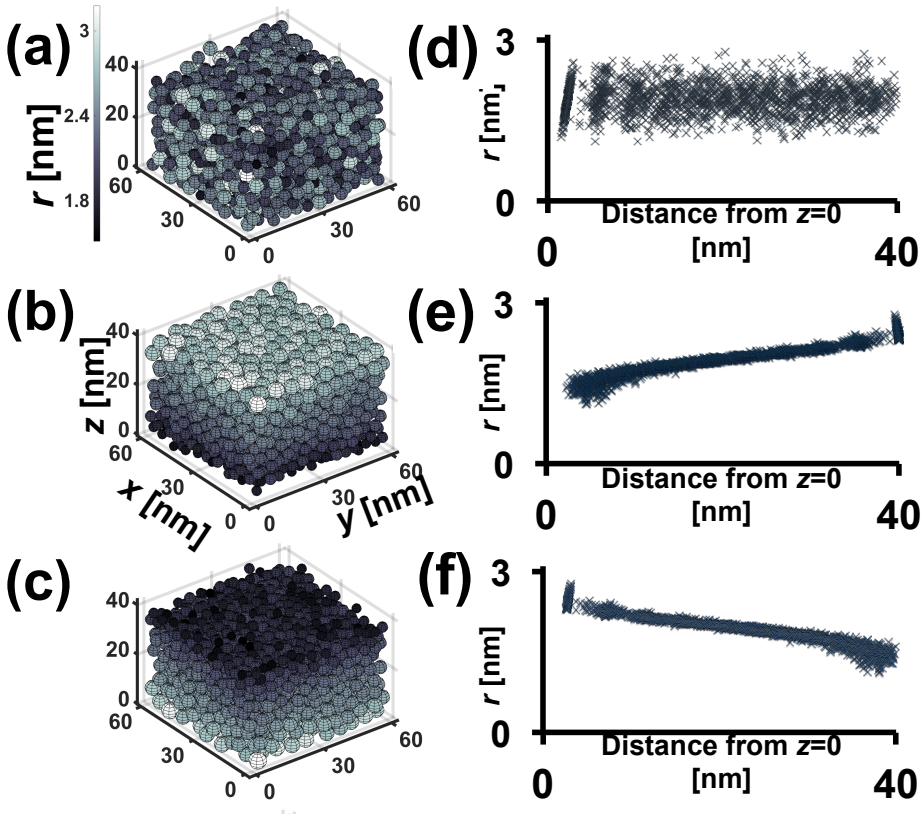

Figure 4-1: Examples of unit cells and radius profiles for the rearranging strategy used in this section: (a)(d) random distribution, (b)(e) ascending radius in $+z$-direction, (c)(f) descending radius in $+z$-direction.

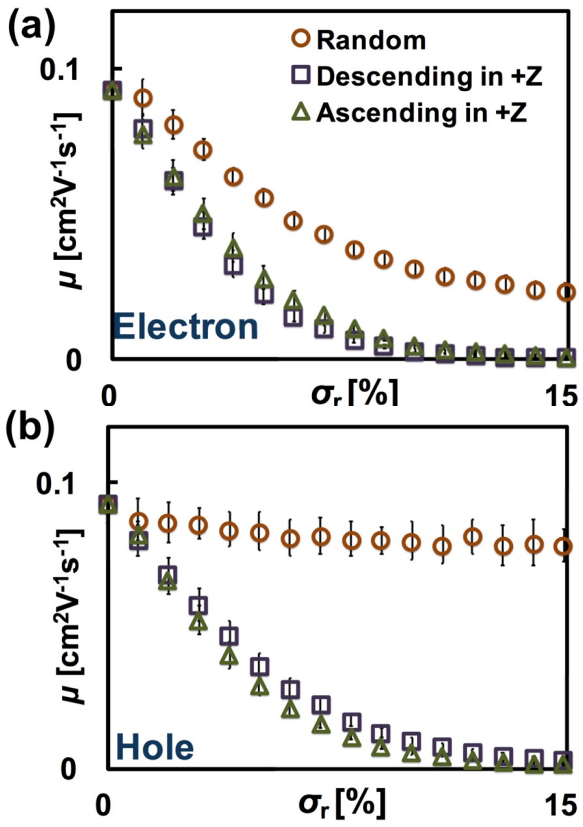

Figure 4-2: Charge carrier mobility ((a) for electrons and (b) for holes) with respect to CQD size dispersion when CQD sizes have ascending or descending order in $+z$-directions; dramatic reductions in mobility are observed for both electrons and holes.

sorting guarantees that those size gradients are generated form the same initial CQD radius distribution for each size dispersion from 0% to 15% used in the previous chapter.

Figure 4-2 shows the dramatic reductions in charge carrier mobility as the size dispersion increases, for both electrons and holes. Contrary to the case of random samples, the CQD films with the descending (ascending) radius gradient impose continuous energy barriers for charge hopping; in the case of descending (ascending) radius gradient, holes (electrons) need extra thermal energy to overcome these energy barriers, which leads to large drops in the charge carrier mobility. Surprisingly, the mobility for opposite charge (electrons for descending radius-gradient samples and holes for ascending radius-gradient samples) shows a large decrease, which is not in-

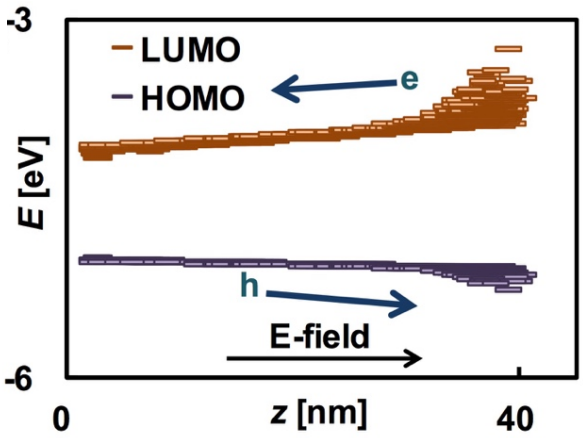

Figure 4-3: The energy diagram (at 15% polydispersity) for a descending case indicates that holes should overcome the energy barrier while electrons travel downhill of energy levels with an electric field in the $+z$-direction.

tuitive from the electric energy diagram shown in Figure 4-3. Electrons (holes) can travel without energy barriers toward the electrode on the left (right) side via CQD networks along a downhill network of energy levels. Equation 2.1 implies that charges hopping from higher energy levels to lower energy levels do not need thermal activation. Therefore, the mobility of the opposite charges should show limited drops or even an improvement for the oriented size dispersion, as opposed to the results we find in Figure 4-2.

In order to elucidate the source of these large and counter-intuitive drops in mobility for both electrons and holes, we prepared a simpler CQD simulation sample with a face-centered-cubic-like (FCC-like) configuration as shown in Figure 4-4(a). When the HOMO-LUMO gaps possess a gradient in the z-direction as in the descending case, the number of charges that show exponential increases along the HOMO-LUMO gap decrease because more electrons can be thermally excited from HOMO to LUMO levels in the case of the smaller energy gaps (See Figure 4-4(b)). Next we separate the impact of energy barrier and diffusion barrier by forcing the limit on each of them. Figure 4-4(c) shows the case where we keep the number of charges constant regardless of HOMO-LUMO gaps. Under positive bias in the $+z$-direction, electrons travel in

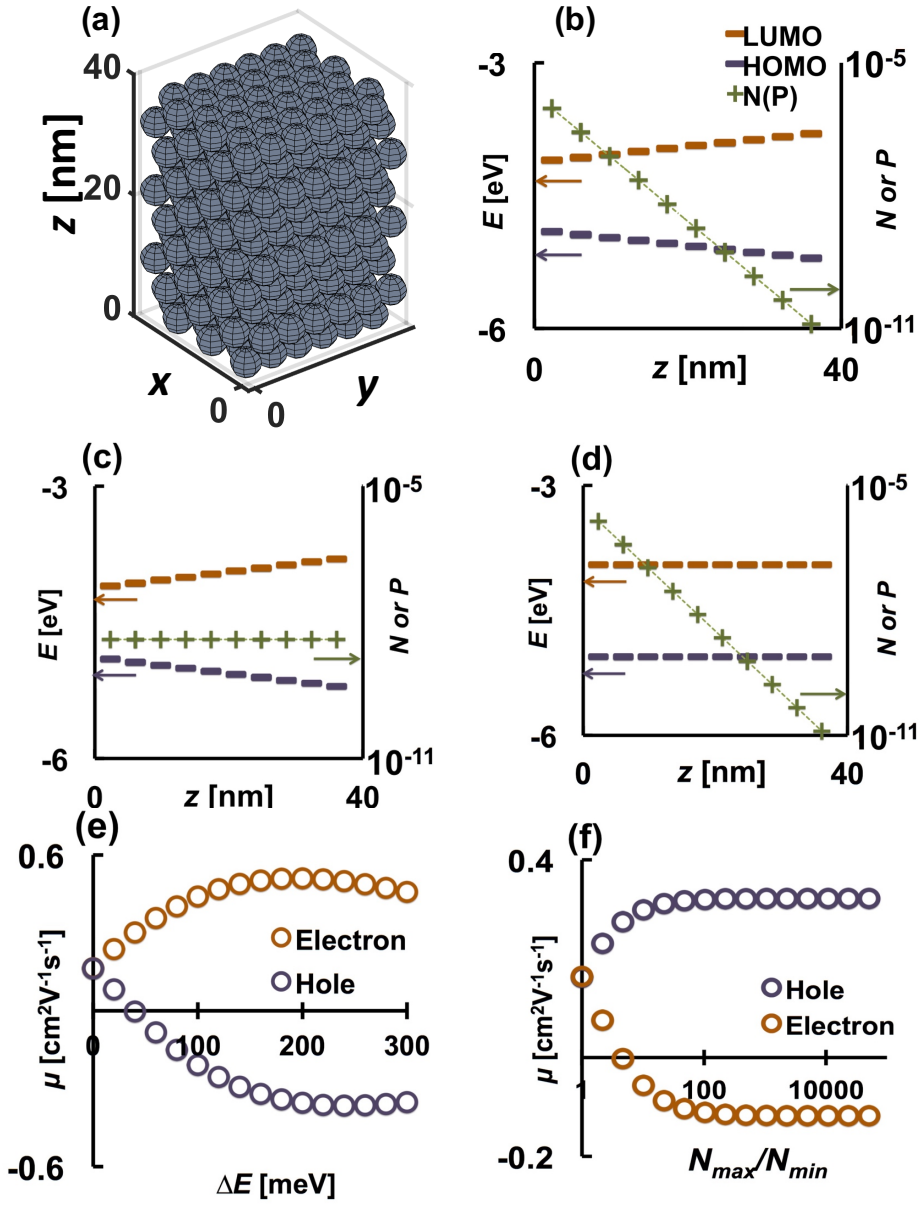

Figure 4-4: Analysis of energy and diffusion barriers with simple CQD simulation sample; (a) a unit cell of the face-centered-cubic-like CQD solid configuration, (b) the distribution of electronic energy levels when sizes of CQDs are sorted along the electric field direction ($+z$). When the number of equilibrium charges is forced to be constant (c) with the same energy level distribution with (b), the energy barriers solely work for hole transport as shown in (e). In the case of constant HOMO-LUMO gaps (d) with the same number of equilibrium charges with (b), diffusion barriers work for electrons that travel in $-z$-direction as shown in (f)

the $-z$-direction without experiencing energy barriers while holes should overcome the thermal energy barriers when they hop toward the electrode near $z = 40$. This contrast in transport behaviors results in complete opposite trends in electron and hole mobility as shown in Figure 4-4(d); as the gradient in HOMO-LUMO gap increases, the hole mobility drops significantly even to negative values, which indicates the positive charges tend to move in the opposite direction of the electric field. In Figure 4-4(e), we show results with constant HOMO-LUMO gaps with exponentially increasing number of charges as the z-position of the CQDs approaches the bias electrode at $z = 0$. Although there is no energy barrier for both electrons and holes in this case under the positive electric field in the $+z$-direction, the result indicates that the electron mobility drops severely when the $N_{max} - to - N_{min}$ ratio increases, where N_{max} (N_{min}) is the maximum (minimum) number of charges in a single CQD in the simulation unit cell. Since Equation 2.1 implies that a donor CQD with large charge population allows higher transport rates, more charge numbers near the bias electrode promotes such a large electron transfer in the $+z$-direction that the electron mobility can turn negative when the gradient in the number of charges is extremely steep. In other words, electrons have to overcome the diffusion barrier from the larger number of electrons in the CQDs "ahead" in the traveling direction. Thus, the significant decreases in charge carrier mobility for both electrons and holes in the case of descending and ascending radius distributions can be attributed to the diffusion barriers as well as energy barriers that serve to simultaneously block transport of all charge carriers. While CQDs with smaller HOMO-LUMO gaps can provide downhill energy pathways that lead to easy charge transport free from energy barriers, a larger number of charges in those smaller gap CQDs will, in turn, prevent those carries from moving freely through the downward energy gradient. These results suggest that the charge distribution in CQD films should be carefully taken into account when designing CQD-based optoelectronic devices where a variety of strategies, including quantum funnel [95] and tandem structures, [10,96] are applied to enhance the device performance. Interestingly, those degradations in charge carrier mobility from the diffusion barriers can be mitigated under the higher electric field as shown in Figure

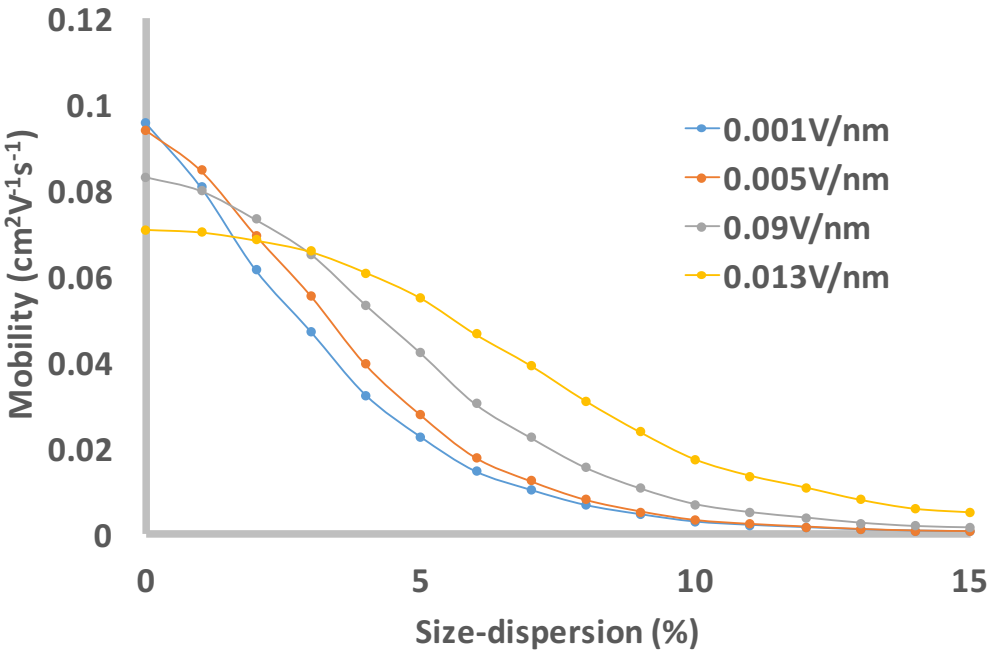

Figure 4-5: The reduced mobility drops at higher electric fields; the diffusion barriers become less significant at high electric field since the charge transport in reverse directions is suppressed by the higher activation energy.

4-5, delivering reduced mobility drops possibly in depletion layers in CQD solar cells or in the field effect transistors working at high electric fields. However, diffusion barriers still considerably prevent efficient charge transfer for the 10% polydisperse case (comparable to $1.5meV/nm$ gradient in energy levels) even at more than 10 times higher electric fields.

Circumventing these coexisting charge transport barriers inevitably requires another method to separate the number of charges and the HOMO-LUMO gap. Figure 4-6 shows that an elaborate doping of CQDs would remove the diffusion barrier effectively. Here, we used FCC-like CQD films where the Fermi levels were set parallel to the LUMO levels by corresponding doping as shown in the dashed line. Note that the first CQD layers near the bias electrode at $z = 0$ were p-doped for the sake of unblocked electron transfer in the $-z$ direction, leading to the invariable electron mo-

bility even for CQD films where high gradients exist in energy levels along the electric field. However, not only would such a strategy require sophisticated additional processes for doping profile control, but it cannot provide fast charge transfer for both electrons and holes simultaneously because the doping profiles induce an imbalance between both electrodes and accumulate a built-in electric field in the $-z$-direction for the case of Figure 4-6, leading to increased energy barriers for holes to travel toward the electrode at $z = 0$. These drawbacks, in turn, call for alternative ways to improve mobility other than CQD radius rearrangement along the electric field direction; in particular, we next explore the potential of horizontal sorting of CQD radii to suppress charge transport rate distracted from the electric field directions.

4.3 Transport Channels with Horizontal Rearrangement

Figure 4-7 shows the examples of unit cells and radius distributions for horizontal rearrangement strategies: (1) an ascending order in size-dispersion as a function of distance from the horizontal center, and (2) a descending order in size dispersion as a function of distance from the horizontal center. While the sorted samples used for the previous section have a gradient in the radii of CQDs, size dispersions rather than radii were controlled in the horizontal directions for these horizontal sorting cases. As seen in the radius profiles in Figure 4-7(c)(d), the redesign of CQD size-dispersion introduces two distinct regions: a monodisperse zone in the center (edge) and CQDs in the edge (center) with smaller or larger than the average size for the ascending (descending) order case.

The trends in carrier mobility for the case where the size dispersion is sorted in horizontal directions are shown in Figure 4-8. Interestingly, the electron mobility shows a smaller drop than the unsorted random cases, bounded at about 40% even when the CQD films have large size dispersions, which indicates that these types of

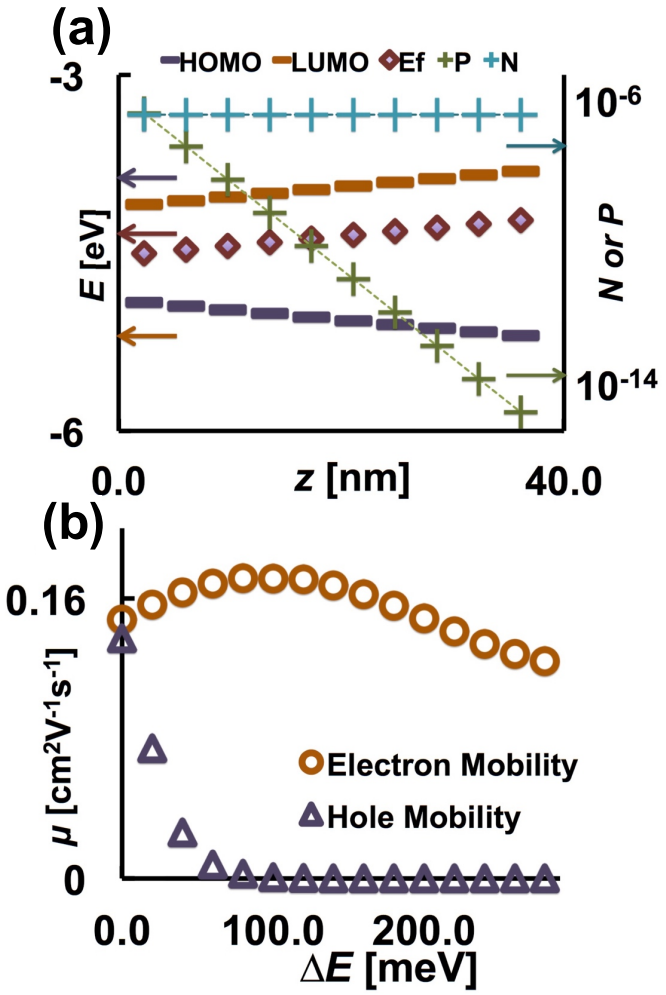

Figure 4-6: (a) Control of the doping profile can circumvent the co-existing energy and diffusion barriers, (b) making mobility for one type of charge (electron for this example) stay high even for a large gradient in the CQD energy levels. The number of electrons is constant for all CQDs since the chemical potentials of electrons are set to be parallel to the LUMO levels while the number of holes is kept same with the sample used in Figure 4-4(b).

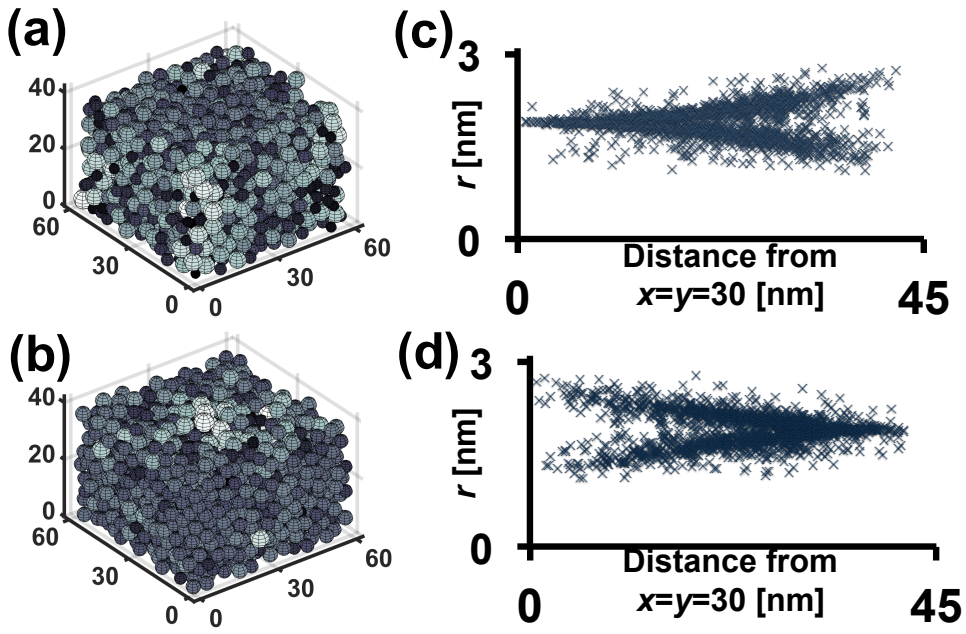

Figure 4-7: Examples of unit cells and radius profiles for the horizontal rearranging strategies: (a)(c) increasing polydispersity as the distance from the center increases, and (b)(d) decreasing polydispersity as the distance from the center increased.

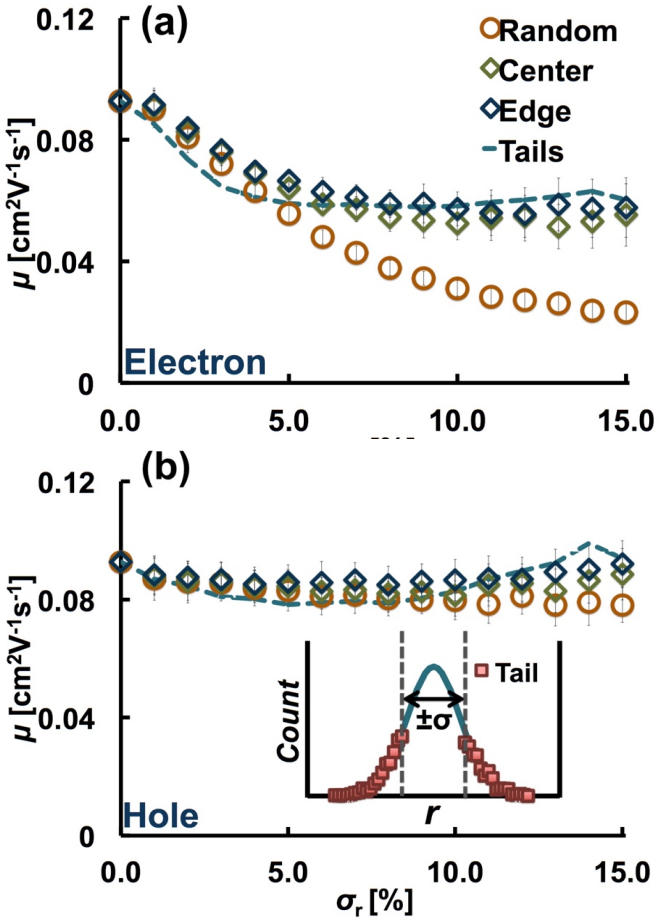

Figure 4-8: Charge carrier mobility for (a) electrons and (b) holes with respect to the CQD size dispersion when CQD films have the size-dispersion gradients in horizontal directions; center (edge) indicate the samples with smaller size dispersion in the center (edge) of the unit cell; and tails indicates the samples with smaller or larger size CQDs than 1-sigma value of the normal distribution as shown in the inset.

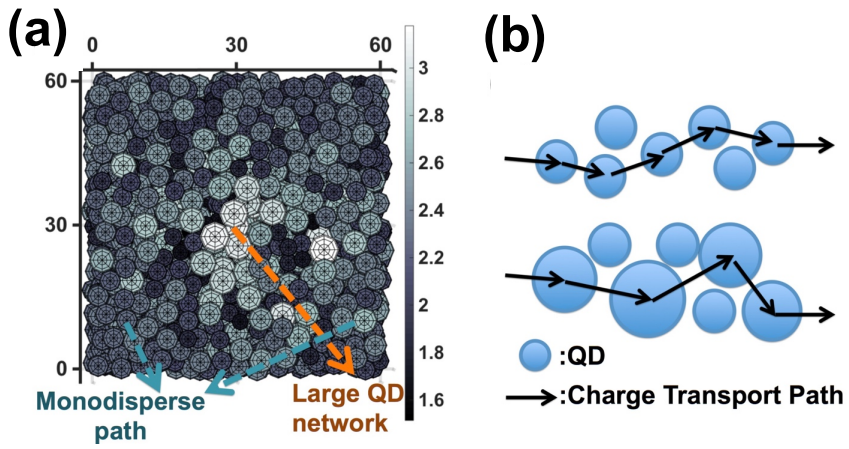

Figure 4-9: Possible paths for higher charge carrier mobility than random cases: (a) cross-section view of the Edge unit cell where the networks of large CQD are in the center, and (b) illustrations of charge hopping transport for small-dispersion path (upper) and the network of large CQDs (lower).

size-dispersion controls may be useful strategies to ease the mobility drop in polydisperse CQD solids. The redesign of size dispersion in horizontal directions leads to the development of two channels through which the charge carriers may move faster than the random cases: smaller disperse paths (Figure 4-9(b), upper) where charge transport stays in the electric field direction as explained earlier, and networks of large CQDs (Figure 4-9(b), lower) where lower site energy differences between larger CQDs bring about higher carrier mobility. [3]

We also confirmed that the latter transport paths actually play effective roles in the mobility enhancement using a simulation cell with 'tail' CQDs that have smaller or larger radii than 1-sigma value of the original normal distribution. The inset in Figure 4-8 shows an example of the radius distribution used. Since the radii of CQDs in each tail sample was generated and selected from the normal distribution sample with originally targeted size-dispersion (1-15%), the actual standard deviation of

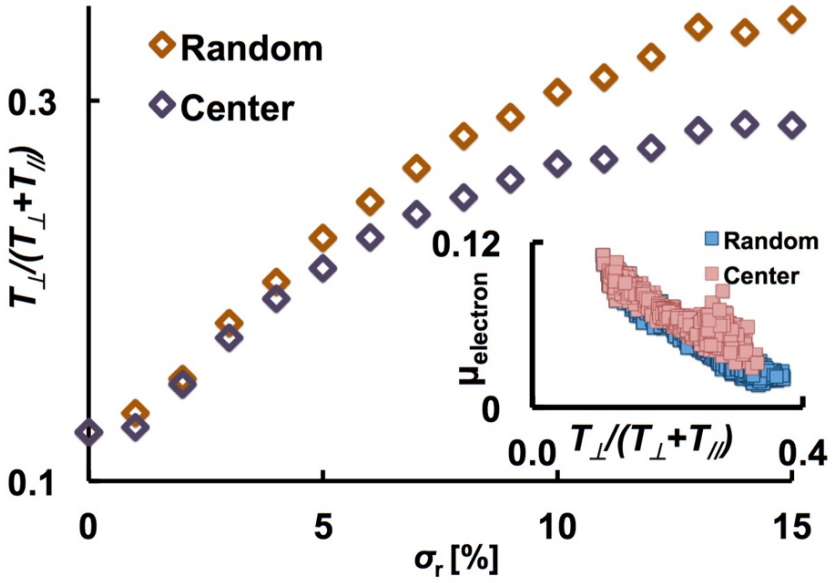

Figure 4-10: The networks of large CQDs promotes the charge transfer along the electric field direction, where comparison in trends of transport rate portions not in the electric field direction between random and Center samples is given; those smaller $T_\perp/(T_\perp + T_{//})$ leads to the higher mobility as shown in the inset.

CQD radii in the tail sample become higher than the original normal distribution. The trends in charge carrier mobility for these tail samples are in good agreement with both cases of horizontal rearrangement of CQD size dispersions. The size-dispersions in the x-axis are from the original distribution for tail samples. Hopping rate vector analysis also confirms that networks of large CQDs played a role in maintaining the lower $T_\perp/(T_\perp+T_{//})$ even at higher size dispersion than that in the randomly arranged CQD solids as shown in Figure 4-10.

Limiting the mobility drops up to 40% with the networks of large CQDs in polydisperse CQD solids, compared to the ≈70% drops in random cases, provides a straightforward improvement in the CQD device performance. For example, the higher mobility would enhance the photovoltaic performance of CQD films, allowing more charge extraction and thicker light absorbing layers. In order to ascertain the impact of spatially tailoring a CQD film to take advantage of the size dispersion, the photovoltaic

performances of those horizontally sorted CQD solids were estimated. Figure 4-11 shows the computed $J-V$ curves for the random and the horizontally sorted 0%, 5%, 10% and 15% polydisperse CQD films with external charge generation. The CQD films with the networks of large CQDs, fitted with dashed lines in Figure 4-11, facilitate efficient charge extraction; 7% and 9% improvement in PCEs were estimated for 10% and 15% polydisperse samples, respectively. Importantly, the percolation networks affect only the current and do not negatively impact the device open circuit voltage. Furthermore, the enhancements in charge extraction increase when thicker CQD films are used as shown in Figure 4-12, indicating that more useful light absorption is available with the improved carrier mobility. The doubled charge carrier mobility expected from the networks of large CQDs at 10% size dispersion enables a roughly 40% enhancement in diffusion length and possible CQD film thickness, leading to a 17%enhanced device performance predicted from the optoelectronic modeling based on experimental data. [37]

Our results suggest that further experimental work toward realizing such design strategies could lead to large improvements in device performance. Despite the successful achievements of well-designed CQD solid structures with size gradients [95] or graded doping [97], the films were deposited using multistep spin-coating processes. In order to apply a CQD radius gradient along the electric field with controlled doping, a new technique combining existing doping controls (mainly from ligand exchanges) and simultaneous size sorting (ex. centrifuging [98]) is needed. On the other hand, the horizontal size-dispersion controls for the networks of large CQDs cannot be achieved without novel methods for separating CQDs with specific sizes. Optical sorting techniques [99–101] can work for this since they change the distribution of nanoparticles with respect to their sizes possibly even during the deposition process; however, further improvements are necessary due to the extremely small size of CQDs and significant solvent flows during the spin-coating. Combination with slower CQD deposition processes such as electrophoresis, [31] Langmuir-Blodgett technique [102] or Langmuir-Schaefer technique [103] can provide scopes for the development of fa-

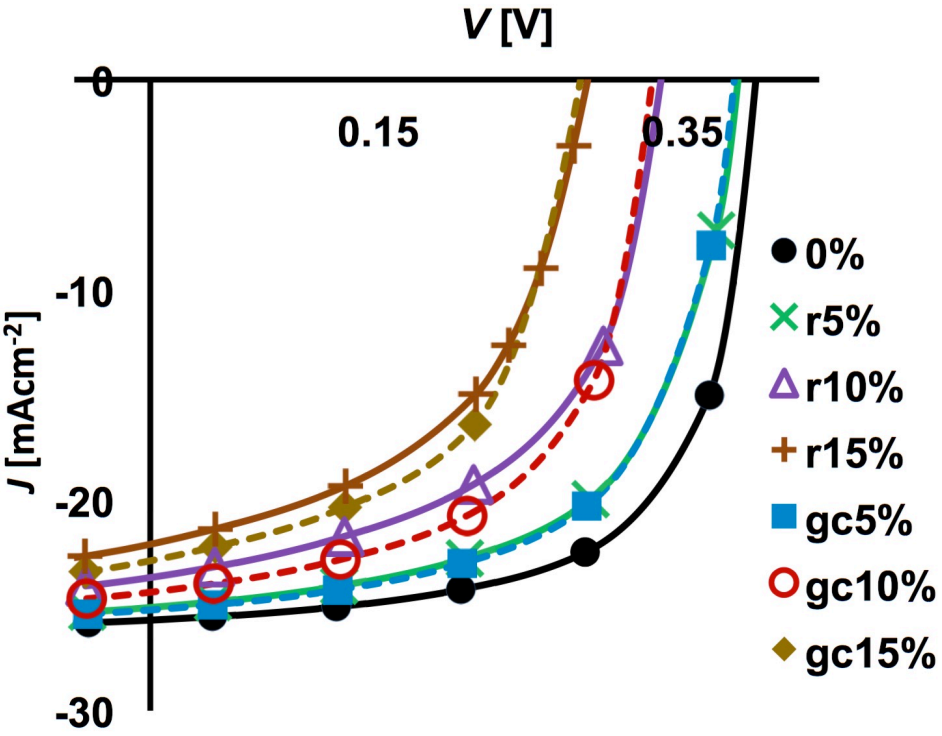

Figure 4-11: Photovoltaic performance of CQD solid with the horizontal sorting strategy; numbers in the indices mean the polydispersity (%) and "r" ("gc") indicates sample with random arrangements (gradient in size dispersion with smaller dispersion in the center). About 10% enhancement in the short-circuit currents was observed with the sorting strategy without change in the open-circuit voltages.

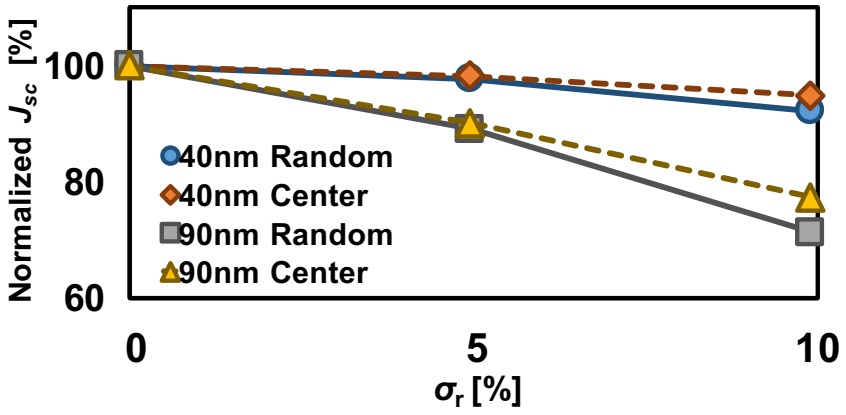

Figure 4-12: Trends in the short-circuit currents, normalized by the value from monodisperse CQD films.

vorable sorting methods.

Chapter 5

Binary CQD model

The enhanced charge carrier mobility in the redesigned CQD solids improved the photovoltaic performances even in the polydisperse cases. Not only does the increased charge extraction ability promote the short circuit current in CQD PV devices, but it also allows the CQD solar cells to utilize thicker light absorbing layers. Meanwhile, the light absorption into thin CQD films can also be improved by use of denser CQD solids with more absorption centers per unit volume. In this chapter, we suggest optimal ways to use two peaks of CQD sizes based on the experimentally suggest CQD solids configurations.

This chapter is written based on the paper *in preparation*: Sangjin Lee and Jeffrey, C. Grossman. Binary CQD solids for improved photovoltaics.

5.1 Binary CQD system

As discussed in Chapter 2, CQD solids deposited from the conventional wet processes possess randomly close-packed configurations and the polydisperse samples we used in the previous chapter were therefore in the same random configurations with packing density of about 0.6. Although 0.74 is the highest packing density available with single-size spheres in an FCC-like stacking, higher packing density (more than 0.82) becomes available if spheres with two sizes fill the space. [104] Applied to the case of CQD solids with two sizes, this denser packing can provide avenues for more efficient light absorption for photovoltaic devices where low charge carrier mobility in CQD layers imposes a limitation on their available thickness. In addition to the inclusion of the higher number of absorption centers, another advantage in using different CQD sizes lies in tuning the absorption spectra using the size-dependent optical response of CQDs. Optical absorbance measured with respect to CQD size, reported in Ref. [1], showed that the discrete electronic energy levels of CQDs induced by the quantum confinement effects forming the 1st excitation peak according to the HOMO-LUMO gaps. We expect the positions of such peaks to be also optimizable so that the CQD films can absorb the solar incident light more efficiently, providing higher generation rates.

Deposition of binary CQD solids has been demonstrated in Ref. [105] where a variety of stoichiometries ($AB_x,\ x = 1, 2, 3, 4, 5, 6, 13$) were self-assembled with slow evaporation processes. In this work the authors found that the inter CQD potentials controlled by their shapes, electric charges, and relative weight regulated the final binary structures. Furthermore, careful selection of ligands also provided densely packed periodic CQD configurations. While a hydrazine-based ligand exchanged was applied to achieve a close-packed CQD assembly, [83] DNA-ligand based self-assembly demonstrated unique arrangements of CQDs. [106] However, the device performance estimation using those binary CQD solids has rarely been reported mainly because a novel device fabrication processes is needed in order to avoid degrading the stability in these structures; it is well known that even the CQD solids having randomly close-

packed configurations are often damaged and cracked in the post processes such as cross-linking and deposition of other layers on top of the existing CQD films. [30]
In order to estimate the potential of binary CQD solids as an excellent light absorption layers for photovoltaic devices and also to provide designs rules for optimal CQD configurations, we applied our hopping transport model to analyze the charge carrier mobility and the optical response to sunlight. Moreover, we will discuss how much enhancement we can obtain in terms of photovoltaic figures-of-merit.

5.2 Charge Carrier Mobility in Binary CQD Solids

Before we estimate the photovoltaic performance of binary CQD solids, we computed the charge carrier mobility in experimentally suggested binary CQD solids. The same simulation conditions were used apart from the CQD solid designs: we changed the size of the larger CQD and the ratio of smaller to large CQD's size. Figure 5-1 shows examples of each binary CQD unit cells and Table 5.1 shows the details of the simulation samples, where A and B indicate the larger and smaller CQD, respectively. The charge carrier mobility for these samples were estimated at 0.001V/nm electric field in the [001] direction of each unit cell. The energy levels were taken from the same experimental results for PbS CQDs as used in the previous chapters. We converged the unit cell size in order not to involve finite size effects from the periodic boundary conditions.

Figure 5-2 shows the trends of electron mobility for the binary CQD samples with respect to the size of the large CQD (r_{A}) and the ratio of the smaller CQD's size to r_{A}. While the mobility decreases by the involvement of smaller CQDs, a common trend observed for all the stoichiometries is that smaller B-CQD sizes in the binary structures promote the efficient charge transport. This trend is explained as the competition between the energetic disorder and the shortened hopping distances. By adding different sizes into the CQD solids, we can expect similar effects as we have seen in the Chapter 3: the mobility drops from the increased site energy. At the same time, involvement of smaller B-CQD forms denser CQD films, reducing the

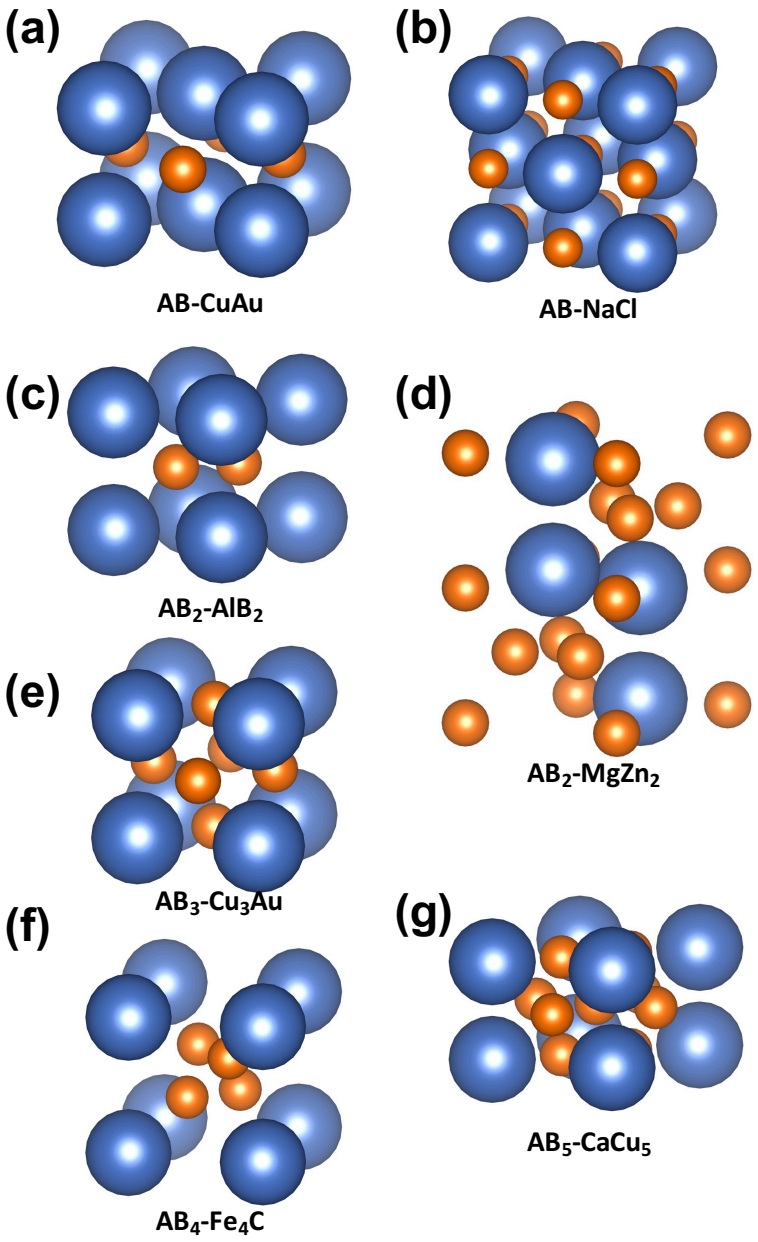

Figure 5-1: Examples of the binary CQD solids used in this chapter. A represents the bigger CQD and B represents the smaller CQD. r_A/r_B is set to 0.5 for all unit cells.

Table 5.1: Binary CQD samples.

Structure	r_A (nm)	r_B / r_A
AB(NaCl)		
AB(CuAu)		
$AB_2(AlB_2)$		
$AB_2(MgZn_2)$	$1.7nm$ - $2.5nm$	0.5 - 0.9
$AB_3(Cu_3Au)$		
$AB_4(Fe_4C)$		
$AB_5(CaCu_5)$		

inter-CQD distances, which consequently provides each CQD with a greater number of available hopping sites nearby. As shown in Figure 5-3, charge carriers mainly transfer through the larger A-CQD, indicating that the reduced distances among A-CQDs play a critical roles in overall charge transport ability in binary CQD system.

While the smaller B-CQD promote charge carrier mobility, the stoichiometry also has a large impact on the charge transport of binary CQD solids. Figure 5-4 shows plots of the electron mobility by the number of B-CQDs in a primitive unit cell for all the binary CQD samples we tested. We observed the smaller number of B-CQDs is favorable for the charge carrier mobility, which is compatible with the fact that the number of larger A-CQDs should be kept high enough since they serve as transport channels.

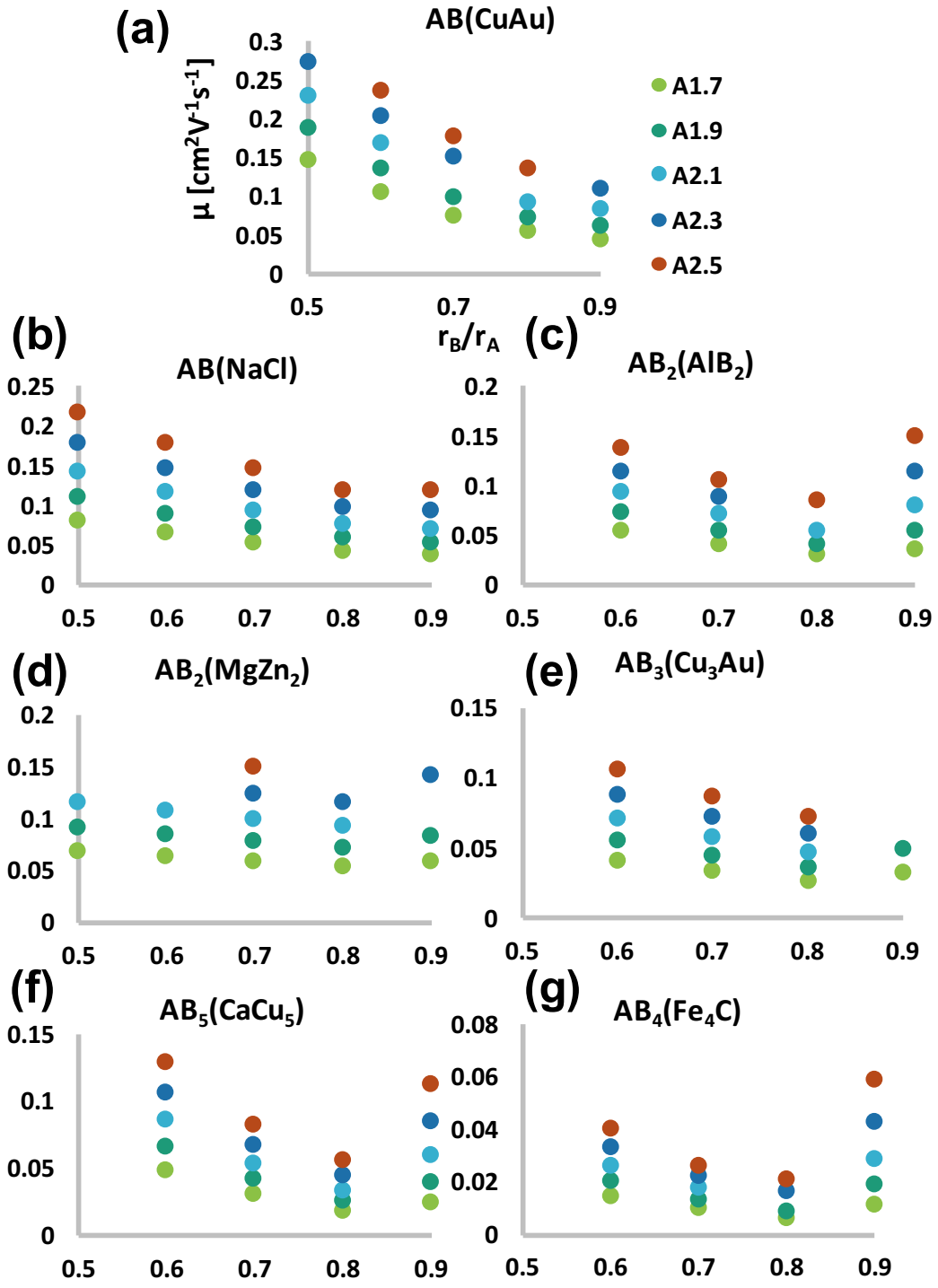

Figure 5-2: The electron mobilities for binary CQD solids where A is the larger CQD and B is the smaller CQD in the primitive unit cell. When B becomes smaller, the electron mobility increased regardless of the structures, which is attributed to the more available hopping states in denser CQD solids.

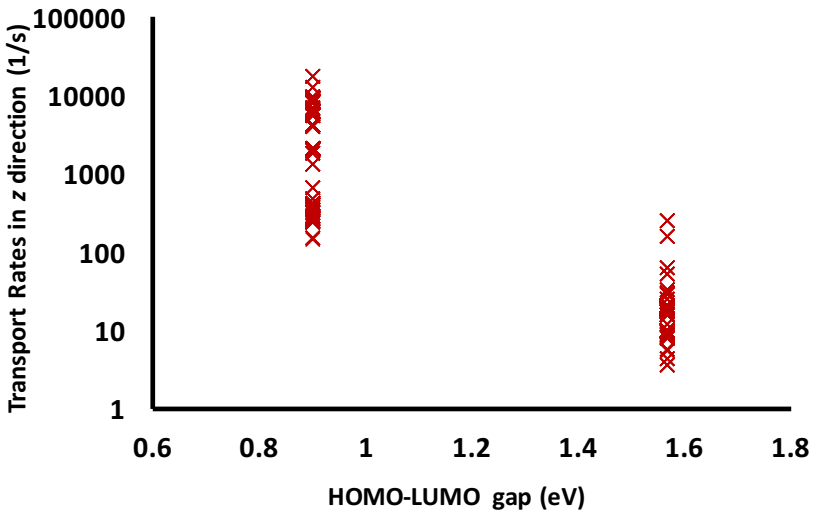

Figure 5-3: Transport rates in z-direction for all CQDs in AB(CuAu) when $r_A = 2.5nm$ and r_B/r_A=0.5; the larger CQD (A) serve as charge transport channels.

5.3 Optical Absorption Model

Using the optimal binary CQD samples based on the trends found in the previous section, we estimate the optical absorption of the binary CQD solids and analyze how much charge generation rates they yield. Given that the binary CQD systems include two different sizes of CQDs placed in the distinct lattice points, an accurate optical absorption model for individual CQDs is required to quantitatively evaluate the optical response as a combined light-absorbing layer in solar cells. Although we used the constant numbers for the external charge generation rates for previous chapters because size-dispersion in CQD solids spreads the absorption spectra, not significantly shifting the peak position, in the case of binary CQD, we should consider size-dependent absorption of CQDs due to the inclusion of two completely different CQD sizes. In other words, G_{ext} in the Equation 2.2 and 2.3 should be handled by taking the size-dependent absorption spectra for two CQD sizes into account for binary CQD layers.

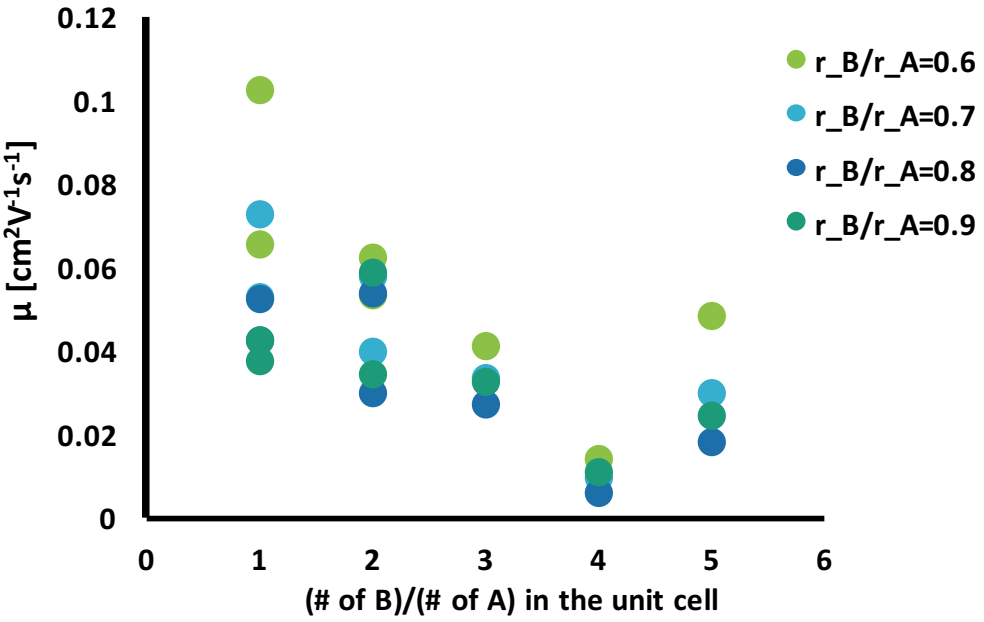

Figure 5-4: The electron mobility with respect to the stoichiometry in a binary CQD solid. The x-axis indicates the ratio of the number of B-CQDs to the number of A-CQD and r_B/r_A in the legend indicates the ratio in their sizes. While B-CQDs may provide denser CQD solids, a given number of A-CQDs is required since the charge transfers mainly via A-CQD networks

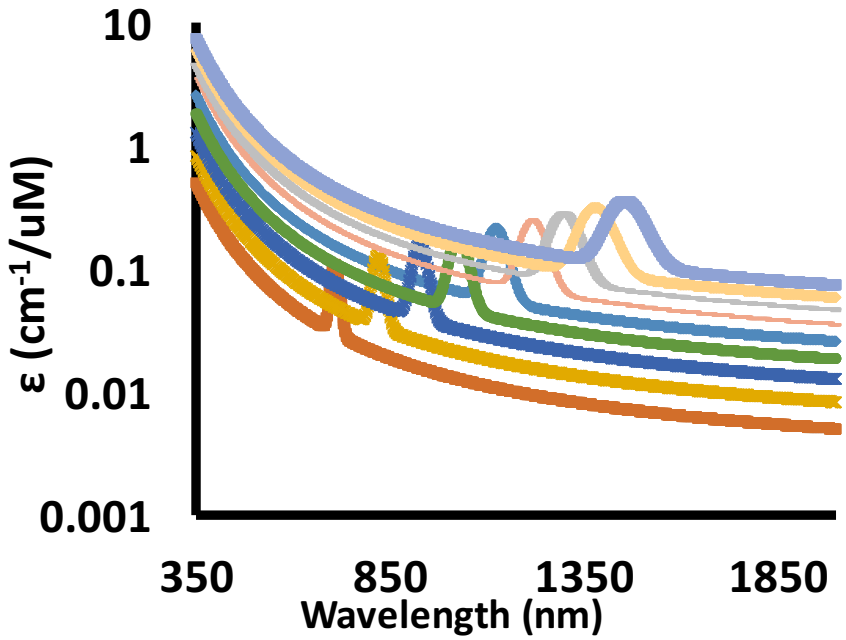

Figure 5-5: The modeled molar extinction coefficient of CQD with different sizes; the oscillation strength at the 1st peak and the absorption coefficient at the higher energy than the 1st peak, where the optical absorption does not show size-dependence, were used from Ref. [1, 4, 5].

5.3.1 Modeling Procedure

We constructed the size-dependent molar extinction coefficient for a single CQD from experimental measurements: the oscillation strength at the 1st peak and the absorption coefficient at far above the peak. [1,4,5] See Figure 5-5 where the molar extinction coefficients are plotted by CQD sizes. Using the Air Mass 1.5 (AM1.5) solar incident energy spectrum, we estimated the absorbance of the CQD solids based on Beer-Lambert law; Equation 5.2 defines the absorbance of each CQD.

$$A_i = \varepsilon_i C_i L_i \tag{5.1}$$

$$I(\lambda, z_2) - I(\lambda, z_1) = -A_i I(\lambda, z_1) \tag{5.2}$$

where the index i represents each CQD, A_i is the absorbance, ε_i is the molar extinction coefficient, C_i is the molar concentration, L_i is the path length of the beam light (comparable to the CQD size), and $I(\lambda, z)$ means the light (wave length λ) intensity at point z as defined in Figure 5-6(a). Tracing the intensity of the incident light in CQD solids, the absorbed energy into each CQD is estimated. Figure 5-6(b) shows an example of the computed absorbed energy when we applied this model to the CQD unit cells with continuously decreasing sizes.

It is noteworthy that the absorbed energies near the oscillations (HOMO-LUMO gap energy) form the peaks at different wavelengths based on the CQD size, which can leads to the optimized solar light absorption. We then estimated the generation rates based on the number of photons absorbed into the CQDs at each wavelength; no multiple exciton generation is assumed. Figure 5-6(c) shows the generation rates computed from the absorbed energy.

5.3.2 Optical Properties of the Binary CQD Solids

The charge generation rates from the solar light absorption, included in equations 2.2 and 2.3, play a critical role in determining the solar cell performance. Not only

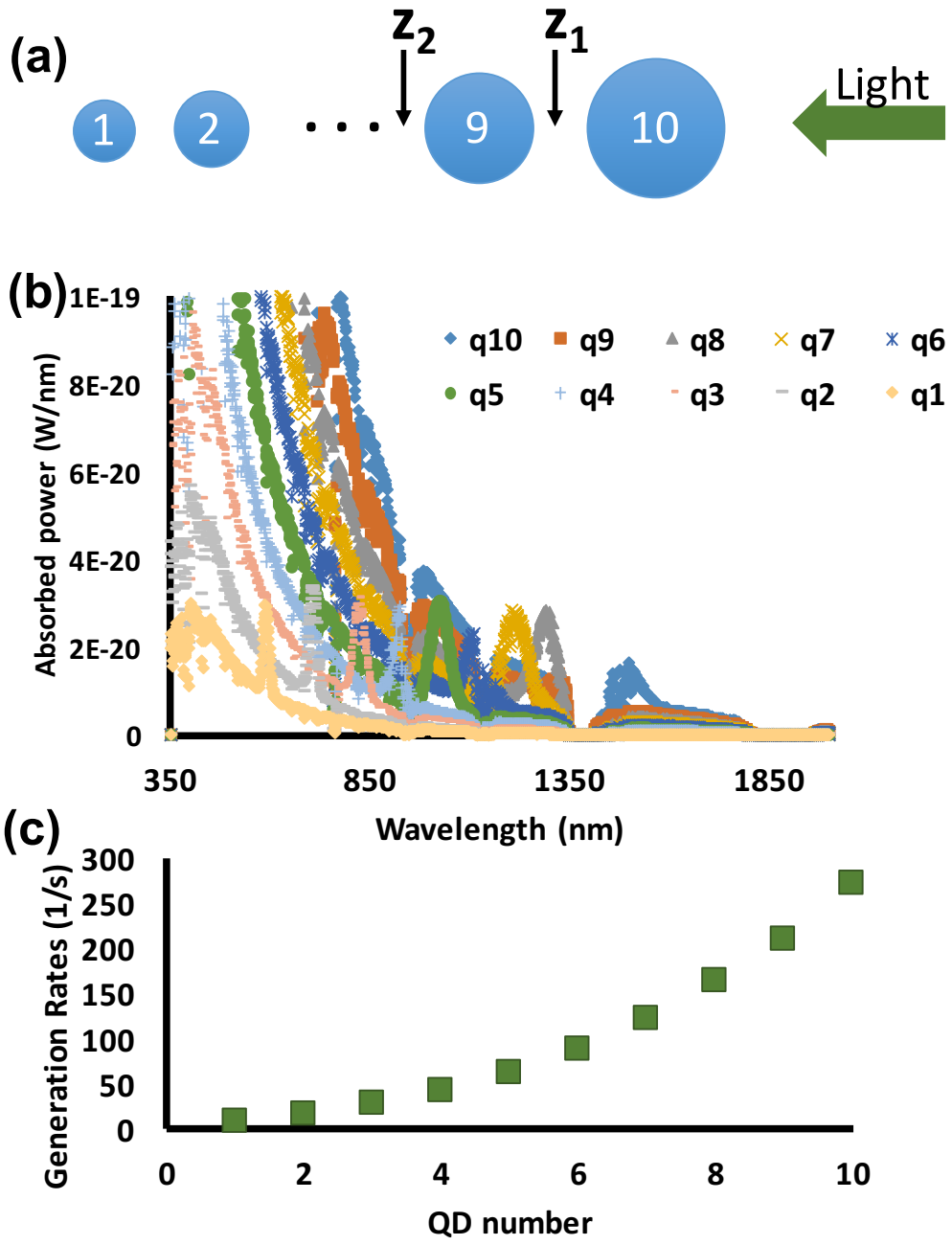

Figure 5-6: A scheme of the optical absorption modeling for CQD solids: (a) arrangement of CQDs for the test, where sizes of CQD decreases along the light path, (b) absorbed power computed from the Air Mass 1.5 incident beam spectrum, and (c) the generation rates for each QD. While the high energy photons are absorbed by larger CQDs at the front of the light path, size-dependent absorptions are observed for the 1st excitation peak energies.

does a high generation rate increase the short-circuit current, but it allows higher enough number of charges so that the split in the quasi Fermi levels can stay large enough, leading to higher open-circuit voltages. In order to analyze the charge generation ability in the binary CQD solids, we computed the generation rates per unit volume based on the size-dependent CQD optical absorption model described in the previous subsection. We chose three binary configurations, AB(NaCl), AB(CuAu) and $AB_5(CaCu_5)$, since they showed the favorable charge transport abilities in Figure 5-4.

Figure 5-7 shows the plots of the average generation rates for AB(NaCl), AB(CuAu) and $AB_5(CaCu_5)$ binary CQDs with respect to the size of the A-CQD and the ratio of the B-CQD size to A-CQD. Interestingly, we observed similar trends with the electron mobility; for example, inclusion of smaller B-CQD enhanced the average generation rates by 39% for the case of 2.5nm A-CQD with 0.5 r_B/r_B in AB(NaCl) structures as shown in Figure 5-7(b). However, the enhancement in the charge generation rates is not only simply from the increase in the packing density; the inset in the Figure 5-7(a) shows the enhancement in the average generation rates is not in complete agreement with that of the packing density. These results imply that not only employing a denser CQD light-absorbing layer is important to improve the solar cell performance, but also different sizes of CQDs with identical chemistry mixed into the same matrix have an impact on the effective charge generations by tuning the absorption spectra along the solar incident spectra. Both factors on the charge generation ability of binary CQD solids, as can be confirmed in Figure 5-8 where we used the random-close packed binary CQD solids with a variety of CQD sizes and stoichiometries. While the strong positive relation indicates the higher packing density boosts the light absorption, spreads in y-axis direction of the average generation rates show that another factor, such as tuned absorption spectra from different sizes, works for efficient light absorption. Tuning in solar-light absorption using completely different CQD chemistry for large differences in absorption peaks, or a rigorous control on the arrangement of two sizes with respect to the light beam directions may further improve the generation rates; for example, AB(CuAu) structures have the

layer-by-layer stacking of A and B CQDs in [001] directions, which can be rotated as [100] directions to become parallel to the light beam for the efficient absorptions, assuming light beams are coming into [001] directions.

5.4 Photovoltaic Performance

We confirmed that there are analogous trends in the charge carrier mobility and the charge generation rates; the binary CQD solids involving the smaller B-CQDs are favorable. In order to estimate how much this strategy can improve the photovoltaic performance, we compute the J-V curves for the selected binary CQD samples. Figure 5-9 shows the J-V curves for solar cells in which AB(NaCl) binary CQD layers are used for light-absorbing layers. The heterojunction structure explained in Chapter 3 was applied with the same positions of the energy levels. The J_{SC} reveals that the smaller B-CQD is favorable for efficient charge generation and extraction as expected from the trends in mobility and generation rates; we confirmed 25% enhancement in J_{SC}.

On the other hand the open-circuit voltages (V_{OC}) do not change much with the size of B-CQDs. As shown in the Figure 5-10, the HOMO-LUMO gaps in A-CQD regulates the V_{OC} while the HOMO and LUMO levels of B-CQDs lie in higher energy states.

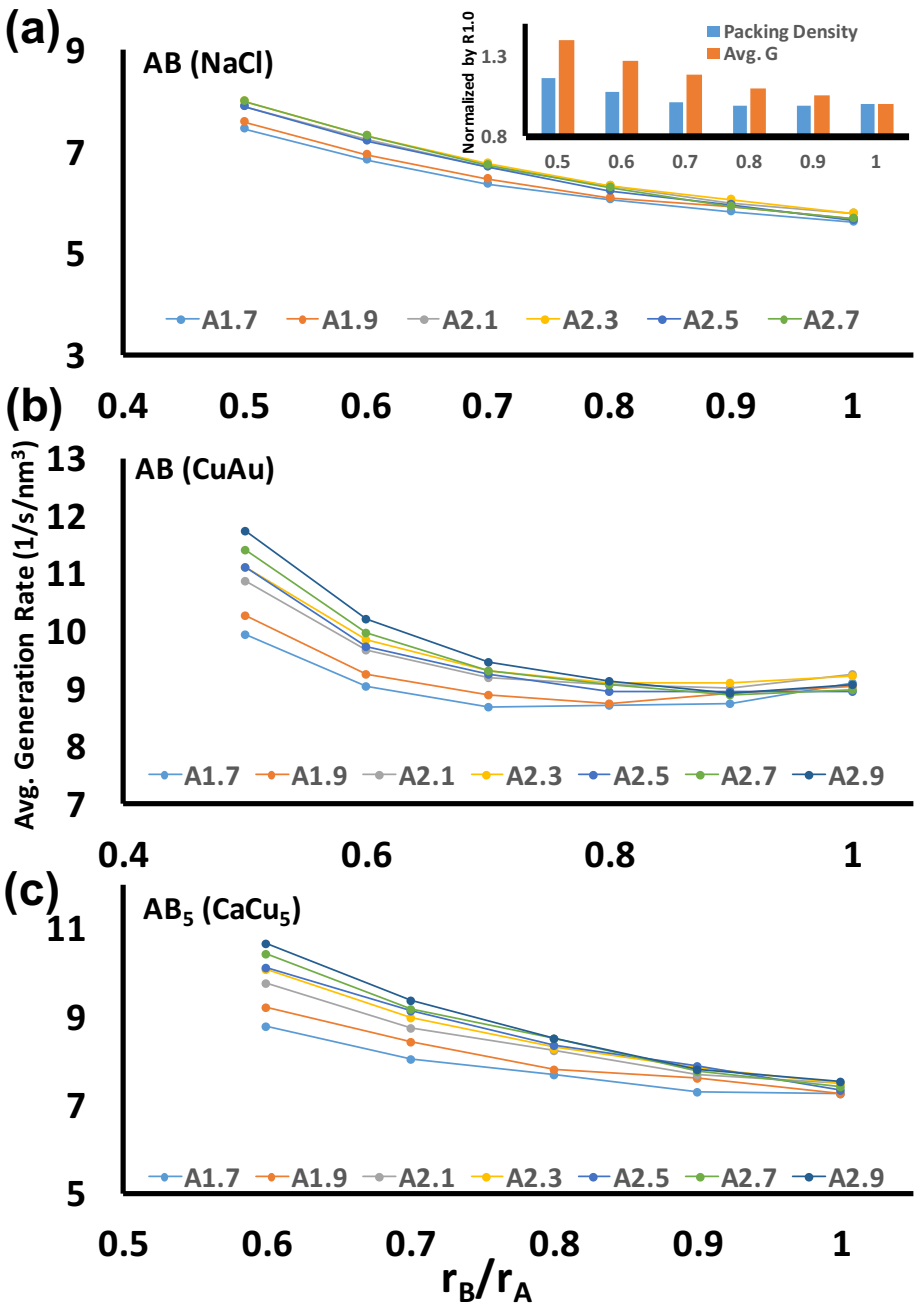

Figure 5-7: Average generation rates for the binary CQD samples for (a) AB(NaCl), (b) AB(CuAu) and (c) $AB_5(CaCu_5)$ with respect to the size ratio. A1.7 indicates that the radius of A-CQD is $1.7nm$. Similar trends with the electron mobility were observed; the inclusion of smaller B-CQD is favorable for efficient optical absorption. The inset in (a) shows the normalized packing densities and the normalized average generation rates for each r_B/r_A for r_A=2.5nm; the enhancement in the average generation rates are not solely from the gain in the packing density.

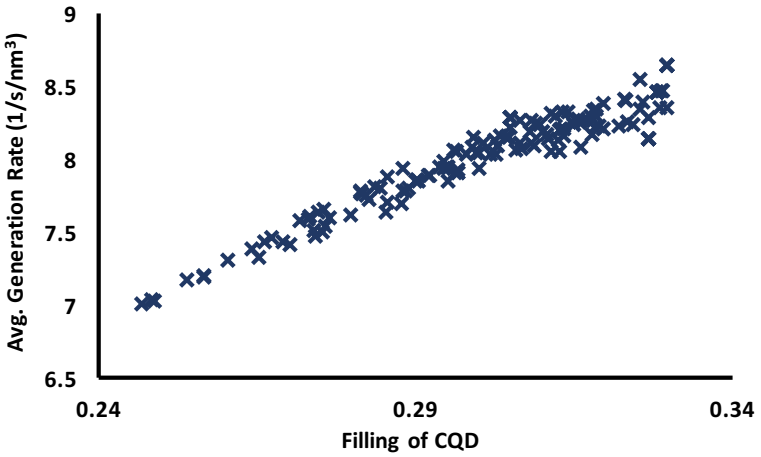

Figure 5-8: Relation between the average generation rates and the packing density for randomly close-packed binary CQD solids; r_A has the range of 1.7-2.9, r_B/r_A has the range of 0.5-0.9, and the number ratio (A to B) has the range of 1-5. While strong positive relation exists, the gain in the average generation rates are not solely from the denser CQD structures.

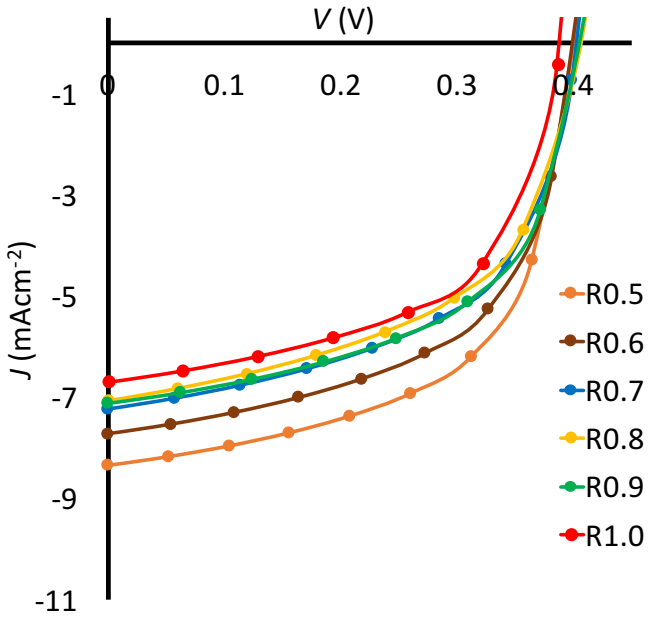

Figure 5-9: The J-V curves for AB (NaCl) binary CQD solids with $r_A = 1.9$. The short-circuit current showed 25% enhancement for the smallest r_B/r_A (R0.5 indicates $r_B/r_A = 0.5$). The open-circuit voltages do not show significant degradation from inclusion of CQDs with different sizes.

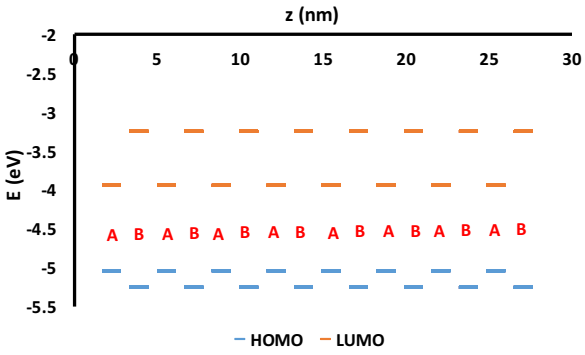

Figure 5-10: Electronic energy diagram for AB(CuAu) binary CQD solids with r_A = 1.9 and r_B/r_A=0.5. Since the open-circuit voltages are limited by the energy levels of the A-CQD, inclusion of smaller B-CQD does not have a significant impact on the open-circuit voltages.

Chapter 6

Conclusion

6.1 Summary

We developed the CQD hopping transport model that can analyze charge transport in CQD solids. The impact of polydispersity on the charge carrier mobility was systematically studied mimicking the experimental CQD film deposition process using MD simulations, which elucidated that more than 70% of electron transport ability has been lost at 10% size dispersion, a typical polydispersity found in CQDs synthesized from the wet-chemistry-process. Those mobility drops significantly degraded the photovoltaic performance of CQD solids in all the figures-of merit, including 34% reduction in PCE. From the redesign of CQD size-dispersion, we confirmed that both the energy and diffusion barriers should be taken into account and those coexisting barriers may degrade the charge transport for electrons and holes for both directions; for circumventing these barrier problems, another properties such as doping profiles should be manipulated carefully. On the other hand, the horizontal rearrangement of size-dispersion successfully moderate the photovoltaic performance degradation by introducing the networks of large CQDs, providing fast charge transport channels. About 10% enhancement in photovoltaic PCE was estimated from polydisperse CQD solids without V_{OC} loss.

Not only does the improved charge carrier mobility promote the short circuit current in photovoltaic devices, it also can allow full solar light absorption by guaranteeing

the efficient charge extraction even in thick absorption layers. While the redesign-of-size-distribution strategies help CQD solar cells involve sufficient thickness of light absorption layer, denser CQD solids with more number of the absorption centers can accelerate the efficient light absorption even in thinner absorption layers. Using the binary CQD solids, we also expected the tunability of CQD optical absorption spectra to the solar incident energy spectra in addition to the effect of denser absorption centers. Adding the size-dependent accurate optical absorption model to the hopping transport code, based on the experimentally reported molar extinction coefficients, we computed the electron mobility and the average generation rates for the binary CQD solids. The similar trends for both optoelectronic properties were observed; not only did the inclusion of smaller CQDs enhance the electron mobility, but it also increased the average generation rates per unit volume. Furthermore, we confirmed that the sufficient charge generation and extraction become available with the binary CQD solid based solar cells where 25% enhancement in the short-circuit current is expected.

6.2 Outlook

While control on ligands and trap states in CQDs has achieved significantly improved charge carrier transport and photovoltaic performance over the last decade, design factors such as polydispersity, arrangement, and periodicity were not explored extensively. In fact, as proved from our estimations in this thesis, re-design of CQD solids can provide an avenue for further enhancement in CQD properties and will play an important role in realization of commercially appealing CQD solar cells.

In order for new designs to be employed, including examples suggested in this thesis, new deposition strategies other than the conventional spin-coatings must be developed. A recent progress in deposition process, such as transfer-printing [30] or centrifuging, [98], is a good example that facilitated more detailed control on CQD arrangement. Furthermore, post-processes for device fabrication, including cross-linking, annealing and deposition of other layers, should be also carefully remodeled

so that CQD solid designs can stay stable; it is well known that defects such as cracks are introduced in CQD solids after these processes. [17, 30]

Our hopping simulation code will be able to provide a better guidance for the experiments as computing power increases. Even though extensive parallelization (a hybrid of shared-memory and distributed-memory parallelization) is applied to our code, estimation of thicker CQD solid requires extremely large amount of computing resources because of a larger number of variables and a longer distance over which the electric field should be integrated. Since computer architectures have been being significantly developing as we can now use more computing power in our mobile devices than supercomputers in 20 years ago, we expect more complicated design factors in a larger scale (for example, the impact of crack and grain boundaries) will be probed in the near future.

6.3 Closing Remarks

As mentioned so far, the CQD hopping transport code we developed grants access to the design factors in CQD solids, which has not been considered a major controller for charge transport and the photovoltaic performance, mainly because there has been no handy way to manipulate the CQD solid designs in experiments. We hope the results in this thesis and our simulation code can provide helpful guides to improve the opto-electronic properties in CQD solids without browsing a large amount of samples with different conditions from scratch in experiments, leading to improved device performance. Although the hopping transport model was used for only PbS CQDs in this thesis, we expect the code can handle a variety of nano-scale materials, not only CQDs with other chemistry but also materials in different dimension such as nanowires and nanorods if charge transport between these nano materials is defined within the hopping regime.

Bibliography

[1] Iwan Moreels, Karel Lambert, Dries Smeets, David De Muynck, Tom Nollet, José C Martins, Frank Vanhaecke, André Vantomme, Christophe Delerue, Guy Allan, and Zeger Hens. Size-dependent optical properties of colloidal PbS quantum dots. *ACS nano*, 3(10):3023–30, oct 2009.

[2] T. S. Mentzel, V. J. Porter, S. Geyer, K. MacLean, M. G. Bawendi, and M. a. Kastner. Charge transport in PbSe nanocrystal arrays. *Physical Review B*, 77(7):1–8, 2008.

[3] Yao Liu, Markelle Gibbs, James Puthussery, Steven Gaik, Rachelle Ihly, Hugh W Hillhouse, and Matt Law. Dependence of carrier mobility on nanocrystal size and ligand length in PbSe nanocrystal solids. *Nano letters*, 10(5):1960–9, may 2010.

[4] Ludovico Cademartiri, Erica Montanari, Gianluca Calestani, Andrea Migliori, Antonietta Guagliardi, Geoffrey A Ozin, Chimica Giaf, V Uni, Via G P Usberti, I Parma, Consiglio Nazionale, Via Gobetti, I Bologna, Istituto Cristallografia Cnr-ic, Via Amendola O, and I Bari. Size-Dependent Extinction Coefficients of PbS Quantum Dots. *Journal of the American Chemical Society*, 128(31):10337–10346, 2006.

[5] Zeger Hens and Iwan Moreels. Light absorption by colloidal semiconductor quantum dots. *Journal of Materials Chemistry*, 22(21):10406, 2012.

[6] C.R. Kagan, C.B. Murray, M. Nirmal, and M.G. Bawendi. Electronic energy transfer in CdSe quantum dot solids. *Physical review letters*, 76(9):1517–1520, feb 1996.

[7] C B Murray, C R Kagan, and M G Bawendi. Self-Organization of CdSe Nanocrystallites into Three-Dimensional Quantum Dot Superlattices. *Science*, 270(November):1335–1338, 1995.

[8] C B Murray, D J Noms, and M G Bawendi. Synthesis and Characterization of Nearly Monodisperse CdE (E=S,Se,Te) Semiconductor Nanocrystallites. *Journal of the American Chemical Society*, 115:8706–8715, 1993.

[9] Jiang Tang and Edward H Sargent. Infrared colloidal quantum dots for photovoltaics: fundamentals and recent progress. *Advanced materials*, 23(1):12–29, jan 2011.

[10] Xihua Wang, GI Koleilat, Jiang Tang, and Huan Liu. Tandem colloidal quantum dot solar cells employing a graded recombination layer. *Nature photonics*, 5:480–484, 2011.

[11] Graham H. Carey, Kang W. Chou, Buyi Yan, Ahmad R. Kirmani, Aram Amassian, and Edward H. Sargent. Materials processing strategies for colloidal quantum dot solar cells: advances, present-day limitations, and pathways to improvement. *MRS Communications*, 3(02):83–90, may 2013.

[12] Jiang Tang, Kyle W Kemp, Sjoerd Hoogland, Kwang S Jeong, Huan Liu, Larissa Levina, Melissa Furukawa, Xihua Wang, Ratan Debnath, Dongkyu Cha, Kang Wei Chou, Armin Fischer, Aram Amassian, John B Asbury, and Edward H Sargent. Colloidal-quantum-dot photovoltaics using atomic-ligand passivation. *Nature materials*, 10(10):765–71, oct 2011.

[13] Joshua J Choi, Yee-Fun Lim, Mitk'el B Santiago-Berrios, Matthew Oh, Byung-Ryool Hyun, Liangfeng Sun, Adam C Bartnik, Augusta Goedhart, George G Malliaras, Héctor D Abruña, Frank W Wise, and Tobias Hanrath. PbSe nanocrystal excitonic solar cells. *Nano letters*, 9(11):3749–55, nov 2009.

[14] Keith W. Johnston, Andras G. Pattantyus-Abraham, Jason P. Clifford, Stefan H. Myrskog, Sjoerd Hoogland, Harnik Shukla, Ethan J. D. Klem, Larissa Levina, and Edward H. Sargent. Efficient Schottky-quantum-dot photovoltaics: The roles of depletion, drift, and diffusion. *Applied Physics Letters*, 92(12):122111, 2008.

[15] Chia-Hao M Chuang, Patrick R Brown, Vladimir Bulović, and Moungi G Bawendi. Improved performance and stability in quantum dot solar cells through band alignment engineering. *Nature materials*, 13(May):796, may 2014.

[16] V. L. Colvin, M. C. Schlamp, and A. P. Alivisatos. Light-emitting diodes made from cadmium selenide nanocrystals and a semiconducting polymer. *Nature*, 370(4):354, 1994.

[17] Kyung-sang Cho, Eun Kyung Lee, Won-jae Joo, Eunjoo Jang, Tae-ho Kim, Sang Jin Lee, Soon-jae Kwon, Jai Yong Han, Byung-ki Kim, Byoung Lyong Choi, and Jong Min Kim. High-performance crosslinked colloidal quantum-dot light-emitting diodes. *Nature photonics*, 3(June):341, 2009.

[18] B. O. Dabbousi, M. G. Bawendi, O. Onitsuka, and M. F. Rubner. Electroluminescence from CdSe quantum-dot/polymer composites. *Applied Physics Letters*, 66(11):1316, 1995.

[19] Benjamin S. Mashford, Matthew Stevenson, Zoran Popovic, Charles Hamilton, Zhaoqun Zhou, Craig Breen, Jonathan Steckel, Vladimir Bulovic, Moungi Bawendi, Seth Coe-Sullivan, and Peter T. Kazlas. High-efficiency quantum-dot light-emitting devices with enhanced charge injection. *Nature Photonics*, 7:407–412, apr 2013.

[20] Jason P Clifford, Gerasimos Konstantatos, Keith W Johnston, Sjoerd Hoogland, Larissa Levina, and Edward H Sargent. Fast , sensitive and spectrally tuneable colloidal- quantum-dot photodetectors. *Nature nanotechnology*, 4:40, 2009.

[21] Gerasimos Konstantatos, Ian Howard, Armin Fischer, Sjoerd Hoogland, Jason Clifford, Ethan Klem, Larissa Levina, and Edward H Sargent. Ultrasensitive solution-cast quantum dot photodetectors. *Nature*, 442(7099):180–3, jul 2006.

[22] Steven a McDonald, Gerasimos Konstantatos, Shiguo Zhang, Paul W Cyr, Ethan J D Klem, Larissa Levina, and Edward H Sargent. Solution-processed PbS quantum dot infrared photodetectors and photovoltaics. *Nature materials*, 4(2):138–42, feb 2005.

[23] L. E. Brus. ElectronâĂŞelectron and electron-hole interactions in small semiconductor crystallites: The size dependence of the lowest excited electronic state. *The Journal of Chemical Physics*, 80(9):4403, 1984.

[24] Edward H. Sargent. Infrared photovoltaics made by solution processing. *Nature Photonics*, 3(6):325–331, jun 2009.

[25] Michal Soreni-Harari, Nir Yaacobi-Gross, Dov Steiner, Assaf Aharoni, Uri Banin, Oded Millo, and Nir Tessler. Tuning energetic levels in nanocrystal quantum dots through surface manipulations. *Nano letters*, 8(2):678–84, feb 2008.

[26] Patrick R Brown, Donghun Kim, Richard R Lunt, Ni Zhao, Moungi G Bawendi, Jeffrey C Grossman, and Vladimir Bulovi. Energy Level Modification in Lead Sul fide Quantum Dot Thin Films through Ligand Exchange. *ACS nano*, 8(6):5863–5872, 2014.

[27] Patrick R Brown, Richard R Lunt, Ni Zhao, Timothy P Osedach, Darcy D Wanger, Liang-Yi Chang, Moungi G Bawendi, and Vladimir Bulović. Improved current extraction from ZnO/PbS quantum dot heterojunction photovoltaics using a MoO3 interfacial layer. *Nano letters*, 11(7):2955–61, jul 2011.

[28] Joseph M Luther, Matt Law, Matthew C Beard, Qing Song, Matthew O Reese, Randy J Ellingson, and Arthur J Nozik. Schottky solar cells based on colloidal nanocrystal films. *Nano letters*, 8(10):3488–92, oct 2008.

[29] Alexi C Arango, David C Oertel, Youfeng Xu, Moungi G Bawendi, and Vladimir Bulovic. Heterojunction Photovoltaics Using Printed Colloidal Quantum Dots as a Photosensitive Layer 2009. *Nano letters*, 9(860), 2009.

[30] TH Kim, KS Cho, EK Lee, SJ Lee, and Jungseok Chae. Full-colour quantum dot displays fabricated by transfer printing. *Nature photonics*, 5(February):176, 2011.

[31] Katherine W Song, Ronny Costi, and Vladimir Bulović. Electrophoretic deposition of CdSe/ZnS quantum dots for light-emitting devices. *Advanced materials (Deerfield Beach, Fla.)*, 25(10):1420–3, 2013.

[32] Joseph M Luther, Jianbo Gao, Matthew T Lloyd, Octavi E Semonin, Matthew C Beard, and Arthur J Nozik. Stability assessment on a 3% bilayer PbS/ZnO quantum dot heterojunction solar cell. *Advanced materials (Deerfield Beach, Fla.)*, 22(33):3704–7, sep 2010.

[33] Mengxia Liu, F. Pelayo García de Arquer, Yiying Li, Xinzheng Lan, Gi-Hwan Kim, Oleksandr Voznyy, Lethy Krishnan Jagadamma, Abdullah Saud Abbas, Sjoerd Hoogland, Zhenghong Lu, Jin Young Kim, Aram Amassian, and Edward H. Sargent. Double-Sided Junctions Enable High-Performance Colloidal-Quantum-Dot Photovoltaics. *Advanced Materials*, N/A:N/A, 2016.

[34] Randy J Ellingson, Matthew C Beard, Justin C Johnson, Pingrong Yu, Olga I Micic, Arthur J Nozik, Andrew Shabaev, and Alexander L Efros. Highly efficient multiple exciton generation in colloidal PbSe and PbS quantum dots. *Nano letters*, 5(5):865–71, may 2005.

[35] Vishal Shrotriya, Jianyong Ouyang, Ricky J. Tseng, Gang Li, and Yang Yang. Absorption spectra modification in poly(3-hexylthiophene):methanofullerene blend thin films. *Chemical Physics Letters*, 411(1-3):138–143, aug 2005.

[36] Ethan J. D. Klem, Dean D. MacNeil, Paul W. Cyr, Larissa Levina, and Edward H. Sargent. Efficient solution-processed infrared photovoltaic cells: Planarized all-inorganic bulk heterojunction devices via inter-quantum-dot bridging during growth from solution. *Applied Physics Letters*, 90(18):183113, 2007.

[37] David Zhitomirsky, Oleksandr Voznyy, Larissa Levina, Sjoerd Hoogland, Kyle W Kemp, Alexander H Ip, Susanna M Thon, and Edward H Sargent. Engineering colloidal quantum dot solids within and beyond the mobility-invariant regime. *Nature Communications*, 5(May):3803, 2014.

[38] S. M. Sze and J. C. Irbin. Resistivity, Mobility and Impurity Levels in GaAs, Ge, and Si at 300K. *Solid-State Electronics*, 11:599–602, 1968.

[39] Emanuele Orgiu, Appan Merari Masillamani, Jörn-Oliver Vogel, Emanuele Treossi, Adam Kiersnowski, Marcel Kastler, Wojciech Pisula, Florian Dötz, Vincenzo Palermo, and Paolo Samorì. Enhanced mobility in P3HT-based OTFTs upon blending with a phenylene-thiophene-thiophene-phenylene small molecule. *Chemical communications (Cambridge, England)*, 48(10):1562–4, feb 2012.

[40] Jay N. Zemel, James D. Jensen, and Richard B. Schoolar. Electrical and Optical Properties of Epitaxial Films of PbS, PbSe, PbTe, and SnTe. *Physical Review A*, 140:330, 1965.

[41] H. E. Spencer and J. V. Morgan. Hole Mobility and Crystal Size in Lead Sulfide Photoconductive Films. *Journal of Applied Physics*, 31(11):2024, 1960.

[42] C Canali, F Nava, G Ottaviani, and C Paorici. Hole and Electron Drift Velocity in CdSe at Room Temperature. *Solid State Communications*, 11:105–107, 1972.

[43] Maksym V Kovalenko, Marcus Scheele, and Dmitri V Talapin. Colloidal nanocrystals with molecular metal chalcogenide surface ligands. *Science (New York, N.Y.)*, 324(5933):1417–20, jun 2009.

[44] Jong-Soo Lee, Maksym V Kovalenko, Jing Huang, Dae Sung Chung, and Dmitri V Talapin. Band-like transport, high electron mobility and high photoconductivity in all-inorganic nanocrystal arrays. *Nature nanotechnology*, 6(6):348–52, jun 2011.

[45] J. J M Van Der Holst, M. A. Uijttewaal, R. Balasubramanian, R. Coehoorn, P. A. Bobbert, G. A. De Wijs, and R. A. De Groot. Modeling and analysis of the three-dimensional current density in sandwich-type single-carrier devices of disordered organic semiconductors. *Physical Review B - Condensed Matter and Materials Physics*, 79(8):1–11, 2009.

[46] L Torsi, a Dodabalapur, Lj Rothberg, Awp Fung, and He Katz. Intrinsic Transport Properties and Performance Limits of Organic Field-Effect Transistors. *Science (New York, N.Y.)*, 272(5267):1462–4, jun 1996.

[47] Heinz Bässler and Anna Köhler. Charge transport in organic semiconductors. *Topics in current chemistry*, 312:1–65, jan 2012.

[48] Hyunwook Song, Youngsang Kim, Heejun Jeong, Mark A Reed, and Takhee Lee. Coherent Tunneling Transport in Molecular Junctions âĂă. *The Journal of Physical Chemistry C*, 114(48):20431–20435, 2010.

[49] Alexander Tikhonov, Rob D. Coalson, and Yuri Dahnovsky. Calculating electron transport in a tight binding model of a field-driven molecular wire: Floquet theory approach. *The Journal of Chemical Physics*, 116(24):10909, 2002.

[50] Seong Ho Choi, Chad Risko, M Carmen Ruiz Delgado, Bongsoo Kim, Jean-Luc Brédas, and C Daniel Frisbie. Transition from tunneling to hopping transport in long, conjugated oligo-imine wires connected to metals. *Journal of the American Chemical Society*, 132(12):4358–68, mar 2010.

[51] Iek-Heng Chu, Marina Radulaski, Nenad Vukmirovic, Hai-Ping Cheng, and Lin-Wang Wang. Charge Transport in a Quantum Dot Supercrystal. *The Journal of Physical Chemistry C*, 115(43):21409–21415, nov 2011.

[52] Allen Miller and Elihu Abrahams. Impurity Conduction at Low Concentrations. *Physical Review*, 120:745, 1960.

[53] R. A. Marcus. CHEMICAL AND ELECTROCHEMICAL ELECTRON-TRANSFER THEORY. *Annual review of physical chemistry*, 15:155, 1964.

[54] Bernard Derrida. Velocity and diffusion constant of a periodic one-dimensional hopping model. *Journal of Statistical Physics*, 31(3):433–450, 1983.

[55] Z. Yu, D. Smith, a. Saxena, R. Martin, and a. Bishop. Molecular geometry fluctuations and field-dependent mobility in conjugated polymers. *Physical Review B*, 63(8):1–9, 2001.

[56] J. Cottaar and P. a. Bobbert. Calculating charge-carrier mobilities in disordered semiconducting polymers: Mean field and beyond. *Physical Review B - Condensed Matter and Materials Physics*, 74:1–6, 2006.

[57] J. Cottaar, L. J a Koster, R. Coehoorn, and P. a. Bobbert. Scaling theory for percolative charge transport in disordered molecular semiconductors. *Physical Review Letters*, 107(13):1–4, 2011.

[58] W. F. Pasveer, J. Cottaar, C. Tanase, R. Coehoorn, P. A. Bobbert, P. W M Blom, M. De Leeuw, and M. A J Michels. Unified description of charge-carrier mobilities in disordered semiconducting polymers. *Physical Review Letters*, 94(20):1–4, 2005.

[59] Hadrien Lepage, Anne Kaminski-cachopo, Alain Poncet, Gilles Carval, Minatec Campus, Grenoble Cedex, Insa Lyon, and Jean Capelle. Simulation of Electronic Transport in Silicon Nanocrystal Solids. *The Journal of Physical Chemistry C*, 116:10873–10880, 2012.

[60] Victor Rühle, Alexander Lukyanov, Falk May, Manuel Schrader, Thorsten Vehoff, James Kirkpatrick, Björn Baumeier, and Denis Andrienko. Microscopic Simulations of Charge Transport in Disordered Organic Semiconductors. *Journal of chemical theory and computation*, 7(10):3335–3345, oct 2011.

[61] J. J M Van Der Holst, F. W A Van Oost, R. Coehoorn, and P. A. Bobbert. Monte Carlo study of charge transport in organic sandwich-type single-carrier devices: Effects of Coulomb interactions. *Physical Review B - Condensed Matter and Materials Physics*, 83(8):1–13, 2011.

[62] N.J. van der Kaap and L.J.A. Koster. Massively parallel kinetic Monte Carlo simulations of charge carrier transport in organic semiconductors. *Journal of Computational Physics*, 307:321–332, 2015.

[63] Dong Yu, Congjun Wang, Brian L. Wehrenberg, and Philippe Guyot-Sionnest. Variable Range Hopping Conduction in Semiconductor Nanocrystal Solids. *Physical Review Letters*, 92(21):216802, 2004.

[64] N.F. Mott. Introductory talk; Conduction in non-crystalline materials. *Journal of Non-Crystalline Solids*, 1:1, 1968.

[65] Gerd Nanz. A Critical Study of Boundary Conditions in Device Simulation Conditions for Isolating Boundaries. *Simulation of semiconductor devices and processes*, 4:321, 1991.

[66] Christopher M Snowden. Semiconductor device modelling. *Rep. Prog. Phys*, 48(August 1984):223, 1985.

[67] Adi Ben-Israel. A Newton-Raphson method for the solution of systems of equations. *Journal of Mathematical Analysis and Applications*, 15(2):243–252, 1966.

[68] Moon Sung Kang, Ayaskanta Sahu, David J Norris, and C Daniel Frisbie. Size- and temperature-dependent charge transport in PbSe nanocrystal thin films. *Nano letters*, 11(9):3887–92, sep 2011.

[69] Heng Liu, Alexandre Pourret, and Philippe Guyot-sionnest. Mott and Efros-Shklovskii Variable Films. *ACS nano*, 4(9):5211–5216, 2010.

[70] Ting Chen, K V Reich, Nicolaas J Kramer, Han Fu, Uwe R Kortshagen, and B I Shklovskii. Metal-insulator transition in films of doped semiconductor nanocrystals. *Nature materials*, 15(November):299–303, 2015.

[71] Moon Sung Kang, Ayaskanta Sahu, David J Norris, and C Daniel Frisbie. Size-dependent electrical transport in CdSe nanocrystal thin films. *Nano letters*, 10(9):3727–32, sep 2010.

[72] Keith W. Johnston, Andras G. Pattantyus-Abraham, Jason P. Clifford, Stefan H. Myrskog, Dean D. MacNeil, Larissa Levina, and Edward H. Sargent. Schottky-quantum dot photovoltaics for efficient infrared power conversion. *Applied Physics Letters*, 92(15):151115, 2008.

[73] Philippe Guyot-Sionnest. Electrical Transport in Colloidal Quantum Dot Films. *The Journal of Physical Chemistry Letters*, 3(9):1169–1175, may 2012.

[74] David Zhitomirsky, Melissa Furukawa, Jiang Tang, Philipp Stadler, Sjoerd Hoogland, Oleksandr Voznyy, Huan Liu, and Edward H Sargent. N-type colloidal-quantum-dot solids for photovoltaics. *Advanced materials (Deerfield Beach, Fla.)*, 24(46):6181–5, dec 2012.

[75] Alexander H Ip, Susanna M Thon, Sjoerd Hoogland, Oleksandr Voznyy, David Zhitomirsky, Ratan Debnath, Larissa Levina, Lisa R Rollny, Graham H Carey, Armin Fischer, Kyle W Kemp, Illan J Kramer, Zhijun Ning, André J Labelle, Kang Wei Chou, Aram Amassian, and Edward H Sargent. Hybrid passivated colloidal quantum dot solids. *Nature nanotechnology*, 7(9):577–82, sep 2012.

[76] Marcus Scheele, David Hanifi, Danylo Zherebetskyy, Slim T Chourou, Stephanus Axnanda, Benjamin J Rancatore, Kari Thorkelsson, Ting Xu, Zhi Liu, Lin-wang Wang, Yi Liu, and a Paul Alivisatos. PbS Nanoparticles Capped with Tetrathiafulvalenetetracarboxylate : Utilizing Energy Level Alignment for E ffi cient Carrier Transport. *ACS nano*, 3:2532–2540, 2014.

[77] Ji-Hyuk Choi, Aaron T Fafarman, Soong Ju Oh, Dong-Kyun Ko, David K Kim, Benjamin T Diroll, Shin Muramoto, J Greg Gillen, Christopher B Murray, and Cherie R Kagan. Bandlike transport in strongly coupled and doped quantum dot solids: a route to high-performance thin-film electronics. *Nano letters*, 12(5):2631–8, may 2012.

[78] Soong Ju Oh, Nathaniel E Berry, Ji-Hyuk Choi, E Ashley Gaulding, Taejong Paik, Sung-Hoon Hong, Christopher B Murray, and Cherie R Kagan. Stoichiometric control of lead chalcogenide nanocrystal solids to enhance their electronic and optoelectronic device performance. *ACS nano*, 7(3):2413–21, mar 2013.

[79] Wenyong Liu, Jong-soo Lee, and Dmitri V Talapin. III âĹŠ V Nanocrystals Capped with Molecular Metal Chalcogenide Ligands : High Electron Mobility and Ambipolar Photoresponse. *Journal of the American Chemical Society*, 135:1349–1357, 2013.

[80] Hao Zhang, Jaeyoung Jang, Wenyong Liu, and Dmitri V Talapin. Colloidal Nanocrystals with Inorganic Halide, Pseudohalide, and Halometallate Ligands. *ACS nano*, 8(7):7359–7369, 2014.

[81] Kaifu Bian, Zhongwu Wang, and Tobias Hanrath. Comparing the structural stability of PbS nanocrystals assembled in fcc and bcc superlattice allotropes. *Journal of the American Chemical Society*, 134(26):10787–90, jul 2012.

[82] Jing Yang, Tao Ling, Wen-Tian Wu, Hui Liu, Min-Rui Gao, Chen Ling, Lan Li, and Xi-Wen Du. A top-down strategy towards monodisperse colloidal lead sulphide quantum dots. *Nature communications*, 4:1695, jan 2013.

[83] Dmitri V Talapin and Christopher B Murray. PbSe nanocrystal solids for n- and p-channel thin film field-effect transistors. *Science (New York, N.Y.)*, 310(5745):86–9, oct 2005.

[84] David Zhitomirsky, Illan J Kramer, André J Labelle, Armin Fischer, Ratan Debnath, Jun Pan, Osman M Bakr, and Edward H Sargent. Colloidal quantum dot photovoltaics: the effect of polydispersity. *Nano letters*, 12(2):1007–12, feb 2012.

[85] David K Kim, Yuming Lai, Benjamin T Diroll, Christopher B Murray, and Cherie R Kagan. Flexible and low-voltage integrated circuits constructed from high-performance nanocrystal transistors. *Nature communications*, 3:1216, jan 2012.

[86] Steve Plimpton. Fast Parallel Algorithms for Short âĂŞ Range Molecular Dynamics. *Journal of Computational Physics*, 117(1995):1–19, 1995.

[87] H. P. Zhang and H. A. Makse. Jamming transition in emulsions and granular materials. *Physical Review E - Statistical, Nonlinear, and Soft Matter Physics*, 72(1):1–12, 2005.

[88] L E Silbert, D ErtaÅ§, G S Grest, T C Halsey, D Levine, and S J Plimpton. Granular flow down an inclined plane: Bagnold scaling and rheology. *Physical review. E, Statistical, nonlinear, and soft matter physics*, 64(5 Pt 1):051302, 2001.

[89] Nikolai V. Brilliantov, Frank Spahn, Jan-Martin Hertzsch, and Thorsten Pöschel. Model for collisions in granular gases. *Physical Review E*, 53(5):5382–5392, 1996.

[90] Zhongwu Wang, Constanze Schliehe, Kaifu Bian, Darren Dale, William a. Bassett, Tobias Hanrath, Christian Klinke, and Horst Weller. Correlating superlattice polymorphs to internanoparticle distance, packing density, and surface lattice in assemblies of PbS nanoparticles. *Nano Letters*, 13(3):1303–1311, 2013.

[91] Byung-ryool Hyun, Yu-wu Zhong, Adam C Bartnik, Liangfeng Sun, Hector D Abrun, Frank W Wise, Jason D Goodreau, James R Matthews, Thomas M Leslie, and Nicholas F Borrelli. Electron Injection from Colloidal PbS Quantum Dots into Titanium Dioxide Nanoparticles. *ACS nano*, 2(11):2206–2212, 2008.

[92] Mark C Weidman, Megan E Beck, Rachel S Hoffman, Ferry Prins, and William A Tisdale. Monodiaperse, Air-Stable PbS Nanocrystals via Precursor Stoichiometry Control. *ACS nano*, 8(6):6363–6371, 2014.

[93] M. J. Anc, N. L. Pickett, N. C. Gresty, J. a. Harris, and K. C. Mishra. Progress in Non-Cd Quantum Dot Development for Lighting Applications. *ECS Journal of Solid State Science and Technology*, 2(2):R3071–R3082, 2012.

[94] Peter M. Allen, Brian J. Walker, and Moungi G. Bawendi. Mechanistic insights into the formation of InP quantum dots. *Angewandte Chemie - International Edition*, 49(4):760–762, 2010.

[95] Ij Kramer, Larissa Levina, and Ratan Debnath. Solar cells using quantum funnels. *Nano Letters*, 11(9):3701–6, 2011.

[96] Pralay K. Santra and Prashant V. Kamat. Tandem-layered quantum dot solar cells: Tuning the photovoltaic response with luminescent ternary cadmium chalcogenides. *Journal of the American Chemical Society*, 135(2):877–885, 2013.

[97] Zhijun Ning, David Zhitomirsky, Valerio Adinolfi, Brandon Sutherland, Jixian Xu, Oleksandr Voznyy, Pouya Maraghechi, Xinzheng Lan, Sjoerd Hoogland, Yuan Ren, and Edward H. Sargent. Graded doping for enhanced colloidal quantum dot photovoltaics. *Advanced Materials*, 25(12):1719–1723, 2013.

[98] Jin Young Kim, Valerio Adinolfi, Brandon R. Sutherland, Oleksandr Voznyy, S. Joon Kwon, Tae Wu Kim, Jeongho Kim, Hyotcherl Ihee, Kyle Kemp, Michael Adachi, Mingjian Yuan, Illan Kramer, David Zhitomirsky, Sjoerd Hoogland, and Edward H. Sargent. Single-step fabrication of quantum funnels via centrifugal colloidal casting of nanoparticle films. *Nature Communications*, 6:7772, 2015.

[99] Petr Jákl, Tomáš Čižmár, Mojmír Šerý, and Pavel Zemánek. Static optical sorting in a laser interference field. *Applied Physics Letters*, 92(16):2013–2016, 2008.

[100] I. Ricárdez-Vargas, P. Rodríguez-Montero, R. Ramos-García, and K. Volke-Sepúlveda. Modulated optical sieve for sorting of polydisperse microparticles. *Applied Physics Letters*, 88(12):121116–1, 2006.

[101] Tomáš Čižmár, Martin Šiler, Mojmír Šerý, Pavel Zemánek, Veneranda Garcés-Chávez, and Kishan Dholakia. Optical sorting and detection of submicrometer objects in a motional standing wave. *Physical Review B - Condensed Matter and Materials Physics*, 74(3):035105, 2006.

[102] Anand Gole, Nikhil R Jana, S Tamil Selvan, and Jackie Y Ying. Langmuir-Blodgett thin films of quantum dots: synthesis, surface modification, and fluorescence resonance energy transfer (FRET) studies. *Langmuir : the ACS journal of surfaces and colloids*, 24(15):8181–8186, 2008.

[103] Karel Lambert, Richard K. Čapek, Maryna I. Bodnarchuk, Maksym V. Kovalenko, Dries Van Thourhout, Wolfgang Heiss, and Zeger Hens. Langmuir-schaefer deposition of quantum dot multilayers. *Langmuir*, 26(11):7732–7736, 2010.

[104] Adam B. Hopkins, Frank H. Stillinger, and Salvatore Torquato. Densest binary sphere packings. *Physical Review E - Statistical, Nonlinear, and Soft Matter Physics*, 85(2):1–19, 2012.

[105] Elena V Shevchenko, Dmitri V Talapin, Nicholas a Kotov, Stephen O'Brien, and Christopher B Murray. Structural diversity in binary nanoparticle superlattices. *Nature*, 439(7072):55–9, jan 2006.

[106] Robert J Macfarlane, Byeongdu Lee, Matthew R Jones, Nadine Harris, George C Schatz, and Chad a Mirkin. Nanoparticle superlattice engineering with DNA. *Science (New York, N.Y.)*, 334(6053):204–8, oct 2011.